CANCER SYSTEMS BIOLOGY APPROACHES FOR DEVELOPING TREATMENT STRATEGIES AGAINST B CELL LYMPHOMA

A Dissertation

Presented to Faculty of the Weill Cornell Graduate School

of Medical Sciences

in Partial Fulfillment of the Requirements for the Degree of

Doctor of Philosophy

by

Wei Du

August 2018

CANCER SYSTEMS BIOLOGY APPROACHES FOR DEVELOPING TREATMENT STRATEGIES AGAINST B CELL LYMPHOMA

Wei Du, Ph.D.

Cornell University 2018

The transformation from normal cells to cancer cells and the maintenance of the malignant state and phenotypes are associated with genetic and epigenetic deregulations, altered cellular signaling responses and aberrant interactions with the microenvironment. This intrinsic complexity of cancer biology calls for novel systems level approaches for understanding tumorigenesis and for developing effective therapeutic strategies. Computational approaches in cancer systems biology embraces this complexity and studies cancer from a systems point of view. In this thesis, we combine various cancer systems biology methodologies including mathematical modeling, statistics and machine learning approaches to study B cell lymphoma biology from two different angles and bring about guidance to treatment strategies. In the first chapter, we present a novel kinetic modeling based computational framework for optimizing combinatorial therapies against chronic active B cell receptor(BCR) signaling in B cell lymphoma. In the second chapter, we describe a Bayesian classifier that's able to stratify cell of origin subtypes of diffuse large B cell lymphoma based on RNA-Seq data, which is predictive of clinical outcomes. We discuss how above computational analysis provides novel methodology for advising therapeutic strategies.

BIOGRAPHICAL SKETCH

Wei Du was born in Beijing, the capital of China. After completing high school education at Beijing No.4 High School in 2008, she entered Peking University majoring in physics and graduated in 2012. Afterwards she started her doctoral training at Physiology, Biophysics and Systems Biology program in Weill Cornell Graduate School of Medical Sciences, supervised by Dr. Olivier Elemento. Her major work during graduate research is the development of a computational model of the B cell receptor signaling pathway which can be used to predict effective and synergistic drug combinations. Besides her research, she entertains as a singer-song writer and has completed an album of 11 original songs.

ACKNOWLEDGEMENTS

First of all, I would like to express my deepest gratitude to my advisor, Dr. Olivier Elemento, for his continuous support of my graduate research and excellent mentorship. He not only offered brilliant scientific guidance but also provided the greatest emotional support that helped me finish my Ph.D. study. It would not be possible to complete this work without his generous help and tremendous patience.

I would also like to thank my committee members: Dr. John Chodera, Dr. Ari Melnick and Dr. Leandro Cerchietti, who offered very valuable insights on my projects over the years.

Thank to all members of Elemento lab for their constructive comments and suggestions on my projects over the years. Special thank to Heng Pan for many helpful discussions.

Thank to my good friends at PKU, Zhen Bi, Quan Zhou, Lixin Sun, Xin Liang, Yunkun Xie, Junwu Huang who offered tremendous emotional support during my Ph.D. training.

Last but not least, I would like to thank my parents who are always loving and supportive.

TABLE OF CONTENTS

LIST OF FIGURES

LIST OF TABLES

CHAPTER ONE INTRODUCTION

1.1 Oncogenic signaling in cancer and targeted therapy

The activation of intracellular signaling pathways in response to environmental stimulus leads to important cell decisions such as proliferation. The amplitude and duration of pathway activation are precisely and robustly controlled by complex regulatory loops to maintain cellular homeostasis. In cancer, activating mutations or deletion of signaling repressors frequently result in sustained and exaggerated pathway activation that drives uncontrolled tumor survival and proliferation. Targeted therapies that use small molecule inhibitors to repress specific signaling pathway members, e.g. kinases, can directly block oncogenic pathway activation and lead to tumor cell death. These targeted therapies are expected to provide improved efficacy and reduced toxicity compared to chemotherapy.

1.2 Complexity of signaling networks limits the effectiveness of single agent targeted therapy and call for usage of combination therapy

Despite the expectation of improved efficacy, clinical application of targeted therapy is facing several challenges such as low response rate and frequently acquired drug resistance. The limited efficacy of single agent targeted therapy is at least partially due to pathway crosstalks and compensatory circuits within signaling networks targeted by these agents(1). Crosstalks and compensatory circuits allow signals to bypass drug

inhibition and reactivate downstream effectors. By simultaneously repressing multiple nodes in a signaling network, combination therapy has the potential to completely extinguish oncogenic signaling and induce more potent and durable treatment response. Thus, novel drug combinations where two or more drugs work cooperatively to suppress corrupted signaling networks need to be identified to achieve maximum therapeutic efficacy. The complexity of signaling networks makes it difficult to simply guess which combinations will be effective and synergistic and which ones will not. Moreover, given the large number of possible drug combinations against complex signaling networks, comprehensive experimental screening – including exploration of multiple dosages – is not practically feasible. Besides, results acquired from such screening may be specific to the cell line tested, thus lacking general applicability to highly variable primary tumors found in patients.

1.3 Computational models of signaling networks for predicting effective combination therapy

Computational models of signaling networks that can accurately reconstruct signaling dynamics *in silico* may represent a useful alternative to experimental screening and trial-and-error experimental investigation. Once proven reliable, these models can be used to exhaustively test the efficacy of a large number of single drug and drug combinations by quantifying signaling output under corresponding network perturbations. Even though computational modeling has been widely used to study the dynamics of signaling network in the past decades, the development of cancer signaling models and its

application to predicting effective combinatorial therapies is still lacking. In the second chapter, we demonstrate the feasibility of this approach using chronic activation of B cell receptor (BCR) signaling in diffuse large B cell lymphoma (DLBCL) as a model system. We adopted a systems biology approach and established a computational framework to optimize anti-DLBCL combinatorial therapy *in silico*. The proposed approach is broadly applicable and can be used for other malignancies driven by aberrantly active signaling pathways.

1.4 Overview of diffuse large B cell lymphoma and stratification of its subtypes

Diffuse large B cell lymphoma is the most prevalent subtype of non-Hodgkin's lymphoma, with patients responding variably to chemotherapy(2). Using gene expression profiling, two distinct subtypes of DLBCL were identified, which associate with different clinical outcome(3). One subtype, termed activated B cell like(ABC) DLBCL, shows gene expression signature of antigen-activated blood B cell. Another subtype, termed germinal center B cell like (GCB) DLBCL, express genes characteristic of germinal center B cells. It was shown that ABC DLBCL was associated with poorer survival upon chemotherapy. A gene expression based classifier was later developed to stratify the two subtypes of DLBCL in microarray datasets(4).

Even though a gene expression based classifier was developed, currently no software is available for implementing it. Secondly, while such classifier was tested on microarray datasets, it is unclear how to apply the classifier to RNA-Seq profiles. In the third

chapter we present a simple R package adapting the original Bayesian classifier to classify ABC vs. GCB DLBCL. Prior to classification we implemented z score normalization of both training and to-be-classified data, which allowed us to classify profiles from different platforms such as microarray and RNA-Seq. We successfully applied this method to a DLBCL RNA-Seq dataset consisting of 68 patients, where the ABC/GCB classification significantly stratified two subgroups with distinct probability of survival. Moreover, we show that RNA-seq-based stratification using our script outperformed stratification based on immunohistochemistry (IHC) analysis. The R package together with training data is available at GitHub: https://github.com/weiduweillcornell/ABC-GCB-classification-R-script.

1.5 Deregulation of B cell receptor signaling and pathogenesis of activated B cell-like subtype of diffuse large B cell lymphoma

The deregulation of B cell receptor (BCR) signaling is central to the pathogenesis of many B cell malignancies. It is especially central in the activated B cell-like subtype of diffuse large B cell lymphoma (ABC DLBCL). ABC DLBCLs exhibit chronic active BCR signaling, and are addicted to constitutive activation of downstream survival and proliferation signals such as NFκB(5). It has recently been found that a subset of the germinal center B cell like(GCB) subtype of DLBCLs are also dependent on BCR signaling through activation of the PI3K/AKT pathway(6). Multiple small molecule inhibitors against BCR signaling were developed and proved effective in killing BCR-

dependent DLBCLs *in vitro* and *in vivo(7-9)*. However when tested in clinical trials, single agent treatments again demonstrated limited responsiveness and efficacy(10), suggesting an urgent need for the design of effective combination therapies.

1.6 Construction of computational model of the BCR signaling network and prediction of effective combination therapy

In the second chapter, we present a kinetic modeling-based computational framework for predicting and optimizing combinatorial therapy against chronic active BCR signaling **(Figure 1.1).** We constructed a detailed kinetic model of the BCR signaling network parameterized by published signaling responses and protein concentrations. Mathematical models of proximal BCR signaling and downstream transcriptional network have been reported(11-13). But to our knowledge, this is the first kinetic model to reconstruct the entire core BCR signaling network *in silico*. Using published drug response data in a BCR signaling-dependent cell line, we trained a tumor growth model which in combination with the kinetic model allowed us to simulate viability response upon various targeted treatments. Under this framework, we exhaustively tested the efficacy and synergism of all possible combinations of inhibition of eleven currently targetable kinases in the BCR signaling network. We discuss how these results pave the way for the discovery of effective drug combinations.

Figure 1.1 Outline of the approach taken in the present study. The central BCR signaling network was constructed based on validated protein-protein interactions from experimental literature. Parameters of molecular reaction kinetics were estimated from phosphorylation time course data and protein concentrations were retrieved from MOPED protein expression database. A phenotypic tumor growth model was trained on cell viability assays of inhibitor treatments to link signaling response to viability outcome. In the end, simulation of the signaling model in combination with the tumor growth model was conducted to optimize treatment strategy. The model's prediction was compared to published drug response data and new prediction-driven hypotheses were tested independently in vitro.

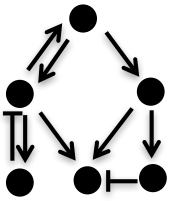

Network construction from experimental literature

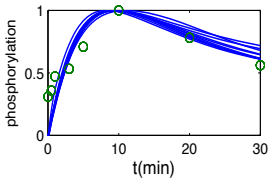

Signaling model parameterization from protein concentration quantification and phosphorylation time course data

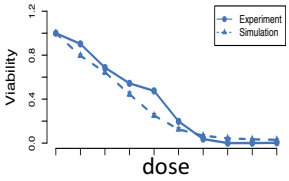

Tumor growth model training from cell line viability assays upon inhibitor treatments

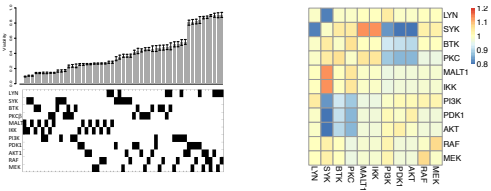

Computational screening to identify potent and synergistic drug combination

LIST OF PUBLICATIONS

1. **Du, W**., Goldstein, R., Jiang, Y., Aly, O., Cerchietti, L., Melnick, A., & Elemento, O. (2017). Effective Combination Therapies for B-cell Lymphoma Predicted by a Virtual Disease Model. *Cancer research*, *77*(8), 1818-1830.

   In this work, I conceived and designed the overall study framework, including selection of computational models, selection of model parameterization methods and design of experiments to validate model's predictions. I developed the computational model, including construction of a core BCR signaling network, development of a kinetic model of the BCR signaling network and integration of a data driven tumor growth model. I performed all the computational analysis including prediction of single and combinatorial drug treatment and computational screening of the most potent and synergistic drug combination. I also analyzed the experimental data.

   This work serves as the main content of the second chapter.

2. **Du,W**.,Pan,H.,Teater,M.,Ghione,P.,Chiapella,A.,Ladetto,M.,Inghirami,G.,Elemento,O.(2017). Predicting ABC vs. GCB Subtypes of Diffuse Large B Cell Lymphoma from RNA-Seq Data. *Under review*

In this work, I developed the computational model and performed all the computational analysis including processing of the RNA-Seq data, model training and testing in microarray dataset and application of the model to RNA-Seq data.

This work serves as the main content of the third chapter.

CHAPTER TWO

EFFECTIVE COMBINATION THEAPIES FOR B CELL LYMPHOMA PREDICTED BY A VIRTUAL DISEASE MODEL

2.1 Kinetic modeling of BCR signaling network reproduces normal BCR signaling *in silico*

We first curated the central BCR signaling network by gathering experimentally validated protein-protein interactions from literature. The reconstructed network is shown in **Figure 2.1**, and includes three major signaling pathways downstream of BCR, namely NFκB, PI3K/AKT and RAF/RAS/ERK. We chose to include these three pathways because they have been reported to closely regulate cell survival and proliferation in B cells and B cell malignancies(14).

Figure 2.1. The central BCR signaling network constructed from literature. Antigen binding induces BCR aggregation and subsequent phosphorylation, which further triggers a complex signaling cascade initiated by phosphorylated LYN and SYK. The BTK-PLCγ2-PKCβ pathway activates downstream NFκB and ERK through divergent paths, while membrane recruitment of PI3K leads to AKT activation. Pathway crosstalks and feedback regulations are highly abundant in the network.

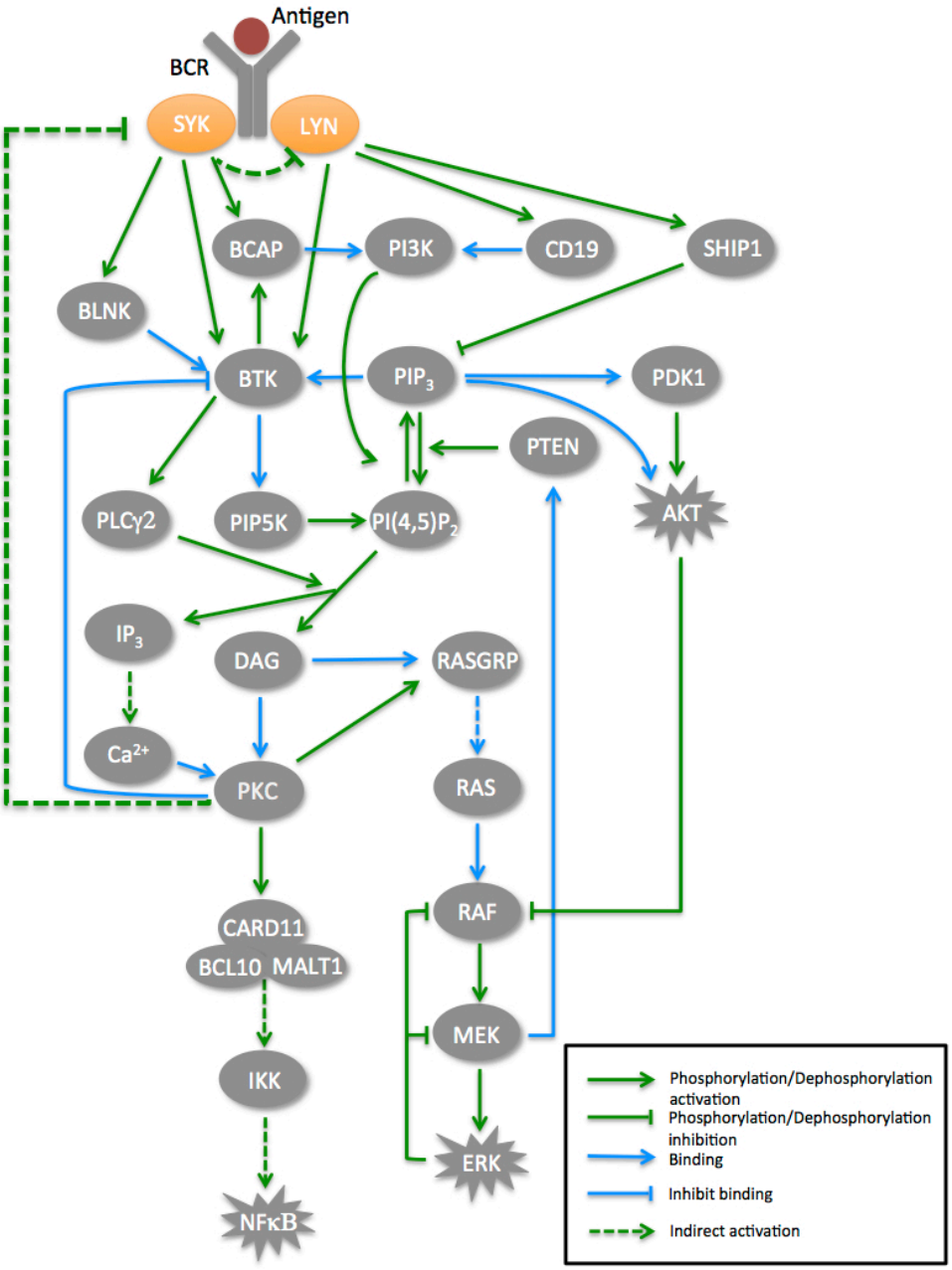
Antigen
BCR
SYK
LYN
BCAP
PI3K
CD19
SHIP1
BLNK
BTK
PIP3
PDK1
PTEN
AKT
PLCγ2
PIP5K
PI(4,5)P2
IP3
DAG
RASGRP
Ca2+
PKC
RAS
CARD11
BCL10
MALT1
RAF
MEK
IKK
ERK
NFκB
Phosphorylation/Dephosphorylation activation
Phosphorylation/Dephosphorylation inhibition
Binding
Inhibit binding
Indirect activation

Antigen-induced BCR crosslinking allows SRC family kinases, mainly LYN, to phosphorylate the immuno-receptor tyrosine based activation motifs (ITAMs) of the intracellular BCR subunits Igα (CD79A) and Igβ (CD79B)(15)**.** Dually phosphorylated ITAM motifs then recruit SYK and activate it via tyrosine phosphorylation(16). Activated SYK phosphorylates adapter BLNK, which recruits BTK to the plasma membrane to facilitate its phosphorylation and subsequent activation by SYK and LYN(17). Activated BTK further phosphorylates PLCγ2, which catalyzes the hydrolysis of phosphatidylinositol-4,5-bisphosphate ($PI(4,5)P_2$) into diacylglycerol (DAG) and inositol trisphosphate (IP_3)(18). DAG together with elevated intracellular calcium induced by IP_3 triggered endoplasmic reticulum (ER) calcium release activates PKCβ(19), which then stimulates two divergent pathways that activate NFκB and ERK respectively. Phosphorylation of CARD11 by PKCβ leads to the assembly of the CBM complex composed of CARD11, BCL10 and MALT1(20). CBM acts as a scaffolding complex that facilitates IKK phosphorylation by TAK1, which in turn phosphorylates IKB and induces its degradation, releasing NFκB into the nucleus to elicit transcriptional activity(21). Additionally, protease activity of MALT1 positively regulates NFκB signaling by cleaving and inactivating inhibitors against NFκB activation such as A20 and RELB(22, 23). In the meantime, PKCβ and DAG activate RASGRP, which triggers the canonical MAPK signaling cascade, leading to eventual phosphorylation and activation of ERK(24). On the other hand, SYK and LYN phosphorylate BCAP and CD19 respectively, which activate PI3K by membrane

recruitment(25, 26). $PI(3,4,5)P_3$ synthesized by PI3K further facilitates PDK1 catalyzed AKT phosphorylation by binding to both proteins via their plextrin homology (PH) domains(27). Importantly, LYN negatively regulates PI3K signaling by activating SHIP1, which hydrolyzes $PI(3,4,5)P_3$ into $PI(4,5)P_2$ (28).

Besides major signal transduction pathways as described above, our model includes key regulatory interactions in the BCR signaling network such as pathway crosstalks and feedback loops. The PI3K pathway positively regulates NFκB and ERK signaling by enhancing BTK membrane recruitment via $PI(3,4,5)P_3$ binding. At the same time, it conversely attenuates ERK signaling via AKT catalyzed RAF phosphorylation(29). It has recently been found that MEK negatively regulates PI3K/AKT signaling by recruiting PTEN to the plasma membrane(30), which dephosphorylates $PI(3,4,5)P_3$ into $PI(4,5)P_2$. BTK amplifies BCR signaling by two coupled positive feedback loops. It recruits PIP5K to the plasma membrane, which produces $PI(4,5)P_2$ to sustain both $PI(3,4,5)P_3$ synthesis and $PI(4,5)P_2$ hydrolysis(31). Additionally, BTK phosphorylates BCAP, further facilitating the membrane recruitment of PI3K(25). The activity of BTK is attenuated by active PKCβ via disruption of its membrane localization, constituting a negative feedback loop(32). Besides, another indirect feedback from PKC to SYK was added into the model as knockdown of PKCδ was shown to mediate hyperphosphorylation of SYK(33). Furthermore, multiple negative feedback loops exist within the MAPK signaling cascade to fine-tune its activation amplitude and duration(34).

Instead of directly applying mass action kinetics to characterize elementary reactions in the network, we chose to adopt more streamlined mathematical representations derived from mass action law under reasonable assumptions. This strategy greatly reduced the number of variables, equations and most importantly parameters required in the mathematical model. As elementary protein-protein binding reactions generally reach equilibrium within seconds, we modeled them by deriving the steady-state relationships from mass action law.

For a reversible protein-protein binding reaction,

$$A + B \underset{k_-}{\overset{k_+}{\rightleftharpoons}} AB \quad (1)$$

at steady-state,

$$[AB] = \frac{k_+}{k_-}[A][B] \quad (2)$$

$$[A] + [AB] = [T_A] \quad (3)$$

$$[B] + [AB] = [T_B] \quad (4)$$

where [A] and [B] stand for the concentration of freed form of A and B; $[T_A]$ and $[T_B]$ stand for the total concentration of A and B; [AB] represents the concentration of the complex. By solving the above three equations, we have

$$[AB] = \frac{(1+K([T_A]+[T_B])) - \sqrt{(1+K([T_A]+[T_B]))^2 - 4K^2[T_A][T_B]}}{2K} \quad (5)$$

where $K = \frac{k_+}{k_-}$, is the inverse of the dissociation constant K_d .

Under a few circumstances where a protein may bind to more than one partner, the interactions were considered independently for simplification.

For enzymatic reactions such as phosphorylation or dephosphorylation, we adopted a classic Michaelis-Menten kinetic framework,

$$\frac{dP}{dt} = \frac{k_{cat}[E][S]}{K_m + [S]} \tag{6}$$

where $\frac{dP}{dt}$ is the rate of catalytic product formation, k_{cat} is the turnover rate, K_m is the Michaelis-Menten constant, [E] and [S] are concentration of enzyme and substrate respectively.

Reactions in the BCR signaling network were written into corresponding equations according to rules discussed above. The full model consists of 28 state variables each representing concentration of a specific form of a protein species, depicted by 10 steady-state equations and 18 ODEs(**Figure 2.2**).

$$\frac{d[pBLNK]}{dt} = \frac{k_{syk}[pSYK]([T_{BLNK}] - [pBLNK])}{K_{syk} + [T_{BLNK}] - [pBLNK]} - \frac{k_{dblnk}[T_{SHP1}][pBLNK]}{K_{dblnk} + [pBLNK]}$$

$$\frac{d[pBCAP]}{dt} = \frac{k_{syk}[pSYK]([T_{BCAP}] - [pBCAP])}{K_{syk} + [T_{BCAP}] - [pBCAP]} + \frac{k_{btk}[pBTK]([T_{BCAP}] - [pBCAP])}{K_{btk} + [T_{BCAP}] - [pBCAP]} - \frac{k_{dbcap}T_d[pBCAP]}{K_{dbcap} + [pBCAP]}$$

$$\frac{d[pCD19]}{dt} = \frac{k_{lyn}[pLYN]([T_{CD19}] - [pCD19])}{K_{lyn} + [T_{CD19}] - [pCD19]} - \frac{k_{dcd19}T_d[pCD19]}{K_{dcd19} + [pCD19]}$$

$$\frac{d[pSHIP1]}{dt} = \frac{k_{lyn}[pLYN]([T_{SHIP1}] - [pSHIP1])}{K_{lyn} + [T_{SHIP1}] - [pSHIP1]} - \frac{k_{dship}[T_{PTP1B}][pSHIP1]}{K_{dship} + [pSHIP1]}$$

$$[BTK] = \frac{(1 + k_{b1}([pBLNK] + [T_{BTK}]) - \sqrt{(1 + k_{b1}([pBLNK] + [T_{BTK}]))^2 - 4k_{b1}^2[pBLNK][T_{BTK}]}}{2k_{b1}(1 + K_{pkbt}[PKC\beta])}$$
$$+ \frac{(1 + k_{b2}([PIP_3] + [T_{BTK}]) - \sqrt{(1 + k_{b2}([PIP_3] + [T_{BTK}]))^2 - 4k_{b2}^2[PIP_3][T_{BTK}]}}{2k_{b2}(1 + K_{pkbt}[PKC\beta])}$$

$$\frac{d[pBTK]}{dt} = \frac{k_{syk}[pSYK]([BTK] - [pBTK])}{K_{syk} + [BTK] - [pBTK]} + \frac{k_{lyn}[pLYN])([BTK] - [pBTK])}{K_{lyn} + [BTK] - [pBTK]} - \frac{k_{dbtk}T_d[pBTK]}{K_{dbtk} + [pBTK]}$$

$$[PI3K] = \frac{(1 + k_{b3}([pBCAP] + [T_{PI3K}]) - \sqrt{(1 + k_{b3}([pBCAP] + [T_{PI3K}]))^2 - 4k_{b3}^2[pBCAP][T_{PI3K}]}}{2k_{b3}}$$
$$+ \frac{(1 + k_{b4}([pCD19] + [T_{PI3K}]) - \sqrt{(1 + k_{b4}([pCD19] + [T_{PI3K}]))^2 - 4k_{b4}^2[pCD19][T_{PI3K}]}}{2k_{b4}}$$

$$\frac{d[pPLC\gamma 2]}{dt} = \frac{k_{btk}[pBTK]([T_{PLC}] - [pPLC\gamma 2])}{K_{btk} + [T_{PLC}] - [pPLC\gamma 2]} - \frac{k_{dplc}[T_{PTP1B}][pPLC\gamma 2]}{K_{dplc} + [pPLC\gamma 2]}$$

$$[PIP5K] = \frac{(1 + k_{b5}([BTK] + [T_{PIP5K}]) - \sqrt{(1 + k_{b5}([BTK] + [T_{PIP5K}]))^2 - 4k_{b5}^2[BTK][T_{PIP5K}]}}{2k_{b5}}$$

$$[PTEN] = \frac{(1 + k_{mept}([pMEK] + [T_{PTEN}]) - \sqrt{(1 + k_{mept}([pMEK] + [T_{PTEN}]))^2 - 4k_{mept}^2[pMEK][T_{PTEN}]}}{2k_{mept}}$$

$$\frac{d[PIP_2]}{dt} = k_{PIP_2} + \frac{k_{pipi}[PIP5K][T_{pip}]}{K_{pipi} + T_{PIP}} + \frac{k_{ptpi}T_{PTEN}[PIP_3]}{K_{ptpi} + [PIP_3]} - \frac{k_{pi3k}[PI3K][PIP_2]}{K_{pi3k} + [PIP_2]}$$
$$- \frac{k_{plpi}[pPLC\gamma 2][PIP_2]}{K_{plpi} + [PIP_2]} - \gamma_{PIP_2}[PIP_2]$$

$$\frac{d[PIP_3]}{dt} = \frac{k_{pi3k}[PI3K][PIP_2]}{K_{pi3k} + [PIP_2]} - \frac{k_{ptpi}T_{PTEN}[PIP_3]}{K_{ptpi} + [PIP_3]} - \frac{k_{shpi}[pSHIP1][PIP_3]}{K_{shpi} + [PIP_3]}$$

$$\frac{d[DAG]}{dt} = \frac{k_{plpi}[pPLC\gamma 2][PIP_2]}{K_{plpi} + [PIP_2]} - \gamma_{dag}[DAG]$$

$$[PKC\beta] = \frac{(1 + k_{dapk}([DAG] + [T_{PKC\beta}]) - \sqrt{(1 + k_{dapk}([DAG] + [T_{PKC\beta}]))^2 - 4k_{dapk}^2[DAG][T_{PKC\beta}]}}{2k_{dapk}}$$

$$\frac{d[pCARD11]}{dt} = \frac{k_{pkc}[PKC\beta]([T_{CARD11}] - [pCARD11])}{K_{pkc} + [T_{CARD11}] - [pCARD11]} - \frac{k_{dcard}T_d[pCARD11]}{K_{dcard} + [pCARD11]}$$

$$[CBM] = \frac{(1 + k_{b6}([pCARD11] + [T_{MALT1}]) - \sqrt{(1 + k_{b6}([pCARD11] + [T_{MALT1}]))^2 - 4k_{b6}^2[pCARD11][T_{MALT1}]}}{2k_{b6}}$$

$$\frac{d[pIKK]}{dt} = \frac{k_{cbik}[CBM]([T_{IKK}] - [pIKK])}{K_{cbik} + [T_{IKK}] - [pIKK]} - \frac{k_{dikk} * T_d * [pIKK]}{K_{dikk} + [pIKK]}$$

$$\frac{d[NF\kappa B]}{dt} = \frac{k_{nfkb}[pIKK]([T_{NF\kappa B}] - [NF\kappa B])}{K_{nfkb} + [T_{NF\kappa B}] - [NF\kappa B]} - \gamma_{nfkb}[NF\kappa B]$$

$$[PDK1] = \frac{(1 + k_{pdk1}([PIP_3] + [T_{PDK1}]) - \sqrt{(1 + k_{pdk1}([PIP_3] + [T_{PDK1}]))^2 - 4k_{pdk1}^2[PIP_3][T_{PDK1}]}}{2k_{pdk1}}$$

$$[AKT] = \frac{(1 + k_{akt}([PIP_3] + [T_{AKT}]) - \sqrt{(1 + k_{akt}([PIP_3] + [T_{AKT}]))^2 - 4k_{akt}^2[PIP_3][T_{AKT}]}}{2k_{akt}}$$

$$\frac{d[pAKT]}{dt} = \frac{k_{pdak}[PDK1]([AKT] - [pAKT])}{K_{pdak} + [AKT] - [pAKT]} - \frac{k_{dakt}T_d[pAKT]}{K_{dakt} + [pAKT]}$$

$$[RASGRP] = \frac{(1 + k_{dara}([DAG] + [T_{RASGRP}]) - \sqrt{(1 + k_{dara}([DAG] + [T_{RASGRP}]))^2 - 4k_{dara}^2[DAG][T_{RASGRP}]}}{2k_{dara}}$$

$$\frac{d[pRASGRP]}{dt} = \frac{k_{pkc}[PKC\beta]([RASGRP] - [pRASGRP])}{K_{pkc} + [RASGRP] - [pRASGRP]} - \frac{k_{drasgrp}T_d[pRASGRP]}{K_{drasgrp} + [pRASGRP]}$$

$$\frac{d[RAS]}{dt} = \frac{k_{rara}[pRASGRP](T_{RAS} - [RAS])}{K_{rara} + T_{RAS} - [RAS]} - k_{ras}[RAS]$$

$$[RAF] = \frac{(1 + k_{raf}([RAS] + [T_{RAF}]) - \sqrt{(1 + k_{raf}([RAS] + [T_{RAF}]))^2 - 4k_{raf}^2[RAS][T_{RAF}]}}{2k_{raf}(1 + K_{erra}[pERK] + K_{akra}[pAKT])}$$

$$\frac{d[pMEK]}{dt} = \frac{k_{rame}[RAF](T_{MEK} - [pMEK])}{K_{rame} + T_{MEK} - [pMEK]} - \frac{k_{dmek}T_d[pMEK]}{K_{dmek} + [pMEK]}$$

$$\frac{d[pMEK^*]}{dt} = \frac{k_{erme}[pERK]([pMEK] - [pMEK^*])}{K_{erme} + [pMEK] - [pMEK^*]} - \frac{k_{dmek^*}T_d[pMEK^*]}{K_{dmek^*} + [pMEK^*]}$$

$$\frac{d[pERK]}{dt} = \frac{k_{meer}([pMEK] - [pMEK^*])(T_{ERK} - [pERK])}{K_{meer} + T_{ERK} - [pERK]} - \frac{k_{derk}T_d[pERK]}{K_{derk} + [pERK]}$$

Figure 2.2 Equations in kinetic model of BCR signaling network

We modeled LYN and SYK as two independent input signals that triggered a downstream response. Their activation kinetics in normal B cells were approximated by double exponential functions where parameters in the functions were estimated by fitting to published phosphorylation time course data(35)(see below).

$$pLYN = f_{LYN} * T_{LYN} * (A * e^{-t/\tau_1} + B * e^{-t/\tau_2}) \quad (7)$$

$$pSYK = T_{SYK} * T_{SYK} * (C * e^{-t/\tau_3} + D * e^{-t/\tau_4}) \quad (8)$$

where T_{LYN} and T_{SYK} are total concentration of LYN and SYK respectively. f_{LYN} and f_{SYK} are the phosphorylated fraction of LYN and SYK respectively. f_{LYN} and f_{SYK} were estimated by fitting to the phosphorylation time course data using a genetic algorithm. A,B,C,D $\tau_1, \tau_2, \tau_3, \tau_4$.were estimated by fitting to the normalized pLYN and pSYK time course(35).

To parameterize the model, we first retrieved protein concentrations in B lymphocytes quantified by mass-spectrometry from the MOPED protein expression database(36) and literature(37, 38) (**Table 2.1**).

Table 2.1 Table of total protein concentration in the kinetic model

Parameter	Description	Reference
$[T_{LYN}] = 1.18\,\mu M$	total concentration of LYN	(36)
$[T_{SYK}] = 3.27\,\mu M$	total concentration of SYK	(36)
$[T_{BLNK}] = 0.65\,\mu M$	total concentration of BLNK	(36)
$[T_{BCAP}] = 0.9\,\mu M$	total concentration of BCAP	(36)
$[T_{CD19}] = 0.83\,\mu M$	total concentration of CD19	(36)
$[T_{SHIP1}] = 2.82\,\mu M$	total concentration of SHIP1	(36)
$[T_{BTK}] = 1.49\,\mu M$	total concentration of BTK	(36)
$[T_{PI3K}] = 0.33\,\mu M$	total concentration of PI3K	(36)
$[T_{PTEN}] = 0.02\,\mu M$	total concentration of PTEN	(36)
$[T_{PLC\gamma 2}] = 2.57\,\mu M$	total concentration of PLCγ2	(36)
$[T_{PIP5K}] = 4.4\,\mu M$	total concentration of PIP5K	(36)
$[T_{PKC\beta}] = 2.5\,\mu M$	total concentration of PKCβ	(36)
$[T_{CARD11}] = 0.3\,\mu M$	total concentration of CARD11	(36)
$[T_{IKK}] = 0.71\,\mu M$	total concentration of IKK	(36)
$[T_{PDK1}] = 0.27\,\mu M$	total concentration of PDK1	(36)
$[T_{AKT}] = 0.2\,\mu M$	total concentration of AKT	(36)
$[T_{NF\kappa B}] = 0.81\,\mu M$	total concentration of NFκB	(36)
$[T_{SHP1}] = 6.9\,\mu M$	total concentration of SHP1	(36)
$[T_{PTPT1B}] = 1.48\,\mu M$	total concentration of PTP1B	(36)
$[T_{RASGRP}] = 1.03\,\mu M$	total concentration of RASGRP	(36)
$[T_{RAS}] = 0.15\,\mu M$	total concentration of RAS	(36)
$[T_{RAF}] = 1.1\,\mu M$	total concentration of RAF	(36)
$[T_{MEK}] = 1.39\,\mu M$	total concentration of MEK	(36)
$[T_{ERK}] = 2.26\,\mu M$	total concentration of ERK	(36)
$[T_{MALT1}] = 0.23\,\mu M$	total concentration of MALT1	(36)
$[T_d] = 1.0\,\mu M$	total concentration of unidentified phosphatase	Estimate
$[T_{PIP}] = 5\,\mu M$	total concentration of PIP	(37)(38)

We then used genetic algorithms to optimize the remaining 72 kinetic parameters within bounded biologically reasonable ranges(39-41) (**Table 2.2)** by minimizing residual sum

of squares between simulated phosphorylation time courses and published western blot data(35).

Table 2.2 Kinetic parameter bounds

Parameter	K_d	k_{cat}	K_m
Range	$0.1\,nM - 1\,mM$	$0.1 - 10^4\,s^{-1}$	$0.1\,nM - 1\,mM$
Reference	(39)	(40)(41)	(39)

Experimental data and simulated results were each normalized to their respective maximum value for comparison. 10 sets of kinetic parameters were identified from 5000 independent runs that fit almost equally well(42). Simulated trajectory under these 10 parameter sets together with phosphorylation time course data are shown in **Fig 2.3**.

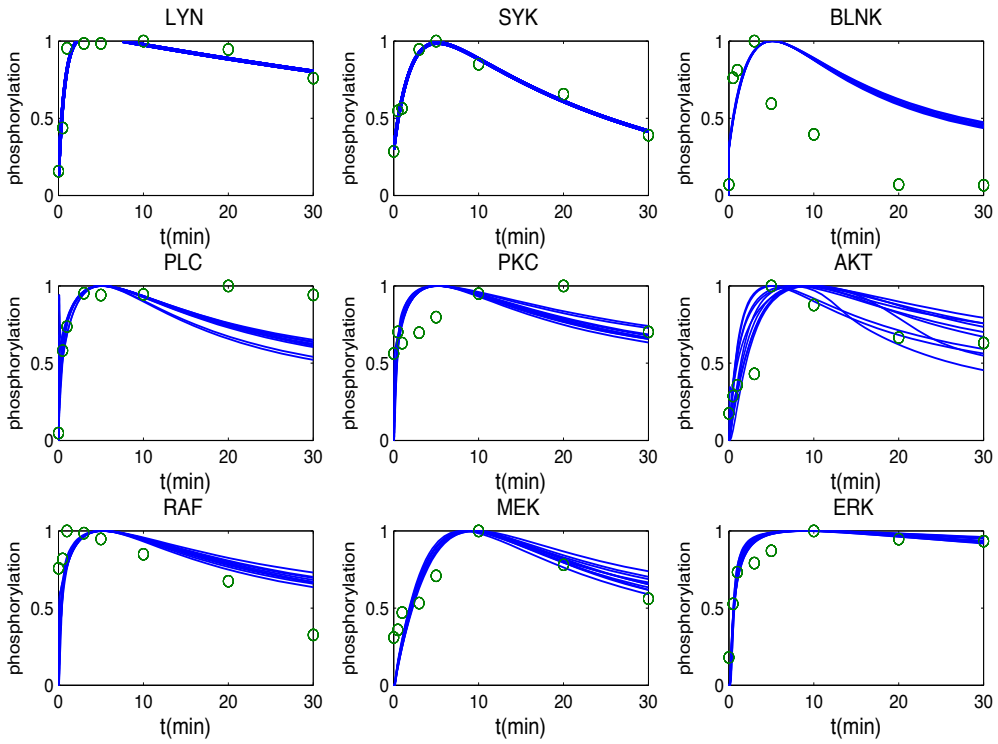

Figure 2.3 Simulated normal BCR signaling. Trajectory of ten parameter sets were shown in comparison with published phosphorylation time course data.

To examine if our fitting method is prone to overfitting problem, we manually injected different levels of white noise into the training time course data and refitted the model using our genetic algorithm. The simulation was done using optimized parameter values as initial population of parameter choice and 10 independent optimization processes were performed for each noise level. We showed that the residual sum of square greatly increases as the noise level increases (**Figure 2.4**). This indicates that the model is not prone to fitting to noise.

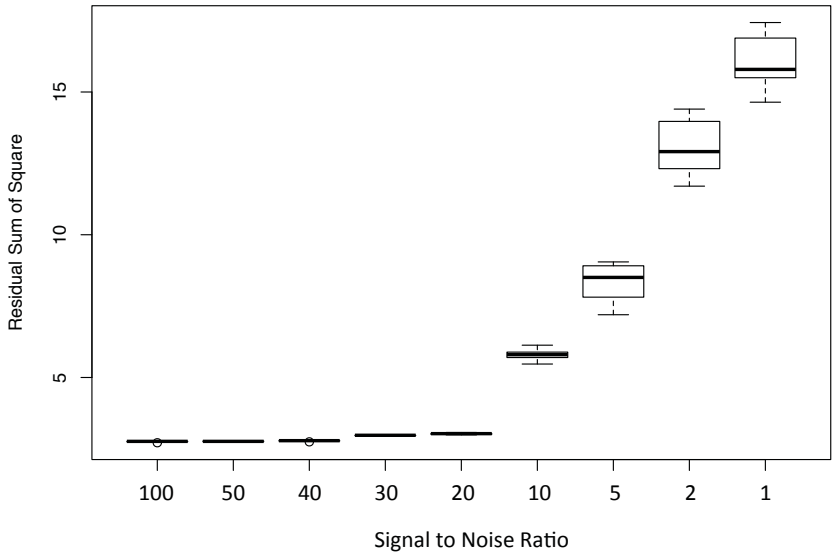

Figure 2.4 Residual sum of square as a function of signal-to-noise ratio

We performed parameter sensitivity analysis where each parameter was perturbed independently across four orders of magnitudes and viability response was recorded. We found overall robustness and identified the most sensitive parameters as parameters regulating main axis of the NFκB pathway(**Figure 2.5**).

Figure 2.5 Parameter sensitivity analysis. Bars show standard deviation of viability response across 4 orders of magnitude perturbation.

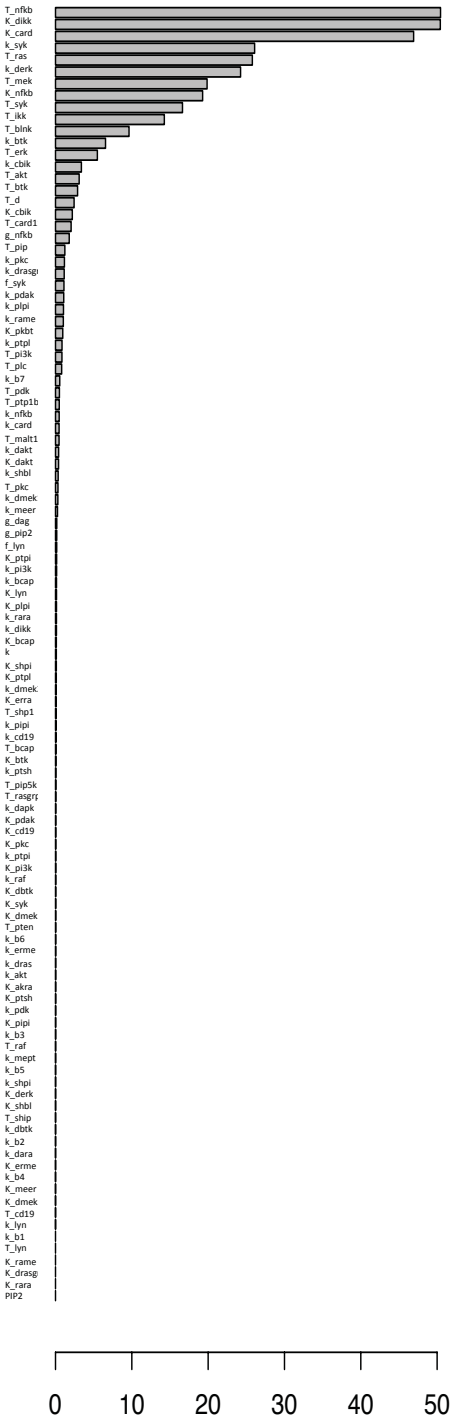
T_nfkb
K_dikk
K_card
k_syk
T_ras
k_derk
T_mek
K_nfkb
T_syk
T_ikk
T_blnk
k_btk
T_erk
k_cbik
T_akt
T_btk
T_d
K_cbik
T_card1
g_nfkb
T_plp
k_pkc
k_drasgı
f_syk
k_pdak
k_plpl
k_rame
K_pkbt
k_ptpl
T_pi3k
T_plc
k_b7
T_pdk
T_ptp1b
k_nfkb
k_card
T_malt1
k_dakt
K_dakt
k_shbl
T_pkc
k_dmek
k_meer
g_dag
g_plp2
f_lyn
K_ptpi
k_pi3k
k_bcap
K_lyn
K_plpi
k_rara
k_dikk
K_bcap
k
K_shpi
K_ptpl
k_dmek
K_erra
T_shp1
k_pipi
k_cd19
T_bcap
K_btk
k_ptsh
T_pip5k
T_rasgrp
k_dapk
K_pdak
K_cd19
K_pkc
k_ptpi
K_pi3k
k_raf
K_dbtk
K_syk
K_dmek
T_pten
k_b6
k_erme
k_dras
k_akt
K_akra
K_ptsh
k_pdk
K_pipi
k_b3
T_raf
k_mept
k_b5
k_shpi
K_derk
K_shbl
T_ship
k_dbtk
k_b2
k_dara
K_erme
k_b4
K_meer
K_dmek
T_cd19
k_lyn
k_b1
T_lyn
K_rame
K_drasg
K_rara
PIP2
0
10
20
30
40
50
standard deviation of viability responses
across 4 magnitudes perturbation

We note that predicted activation time course of BLNK, PLC and PKC deviate from experimental data. We believe that the most likely reason behind this relatively poor fit may be currently unknown regulatory interactions involving additional proteins in the BCR signaling pathway. However the relatively poor fit in these components in the upstream of NFκB pathway would not significantly influence the model's predictions as our parameter sensitivity analysis indicates viability response is most sensitive to parameters in the downstream part of the NFκB pathway (**Figure 2.5**). Of note, we were independently able to find 39 kinetic parameter values from the literature(42), and we compared these values with the range of estimated 10 parameter sets (**Figure 2.6**). By shuffling the literature-retrieved parameters 10,000 times, we found that the literature-retrieved parameter values fall within the estimated parameter ranges significantly more often than random (p=0.05)(**Figure 2.7**). We note however that many discrepancies were found between estimated and published parameters (**Figure 2.6**). We speculate that many of these discrepancies are likely due to *in vitro* nature of the experiments used to quantify kinetic parameters.

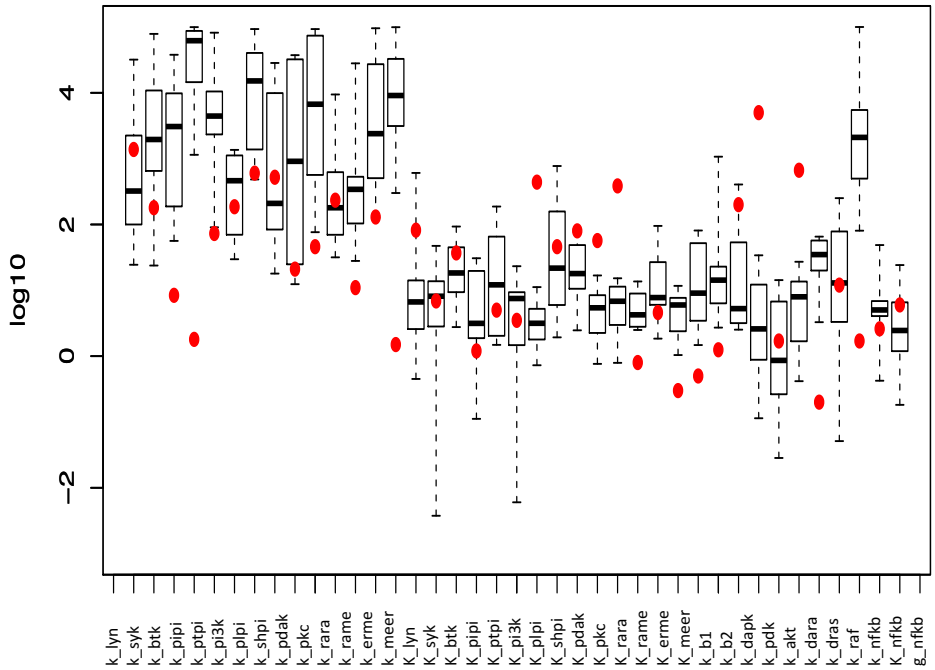

Figure 2.6 Comparison between literature-retrieved parameter values with simulation-estimated parameter ranges. Box-plot indicates the simulation-estimated parameter ranges while red dots represent literature-retrieved parameter values.

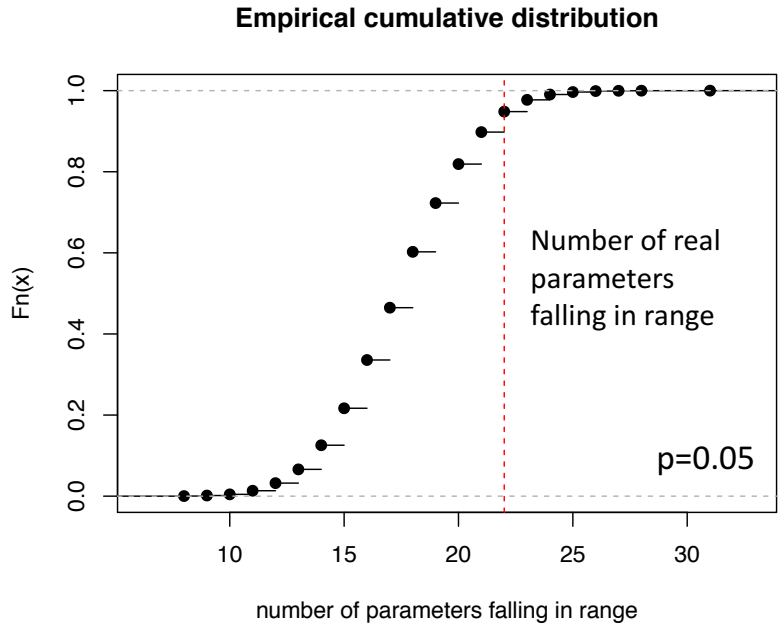

Figure 2.7 Empirical cumulative distribution of the number of parameters that would fall within simulation-estimated parameter ranges by chance derived by shuffling the literature-retrieved parameters 10,000 times.

1.2 Combining BCR signaling model with a tumor growth model predicted cell viability response upon single and combinatorial drug treatments in a BCR signaling-dependent ABC DLBCL cell line

We next sought to simulate the effect of various small molecule inhibitors on ABC DLBCL cell viability and to compare simulation results with published drug response data in a BCR signaling dependent ABC-DLBCL cell line TMD8(43). We selected TMD8 because of the extensive drug combinatorial data available on this cell line(43).

We first made several modifications to the model to accommodate the differences between normal BCR signaling and aberrant BCR signaling in ABC DLBCL. Instead of applying a temporal upstream stimulus, we assumed constitutive LYN and SYK phosphorylation as observed both in ABC DLBCL cell lines and in primary DLBCL patient samples(5, 44). Additionally, we accounted for genetic alterations in members of the BCR signaling network in TMD8 compared to normal B cells. Specifically, TMD8 was shown to carry CD79B mutation that attenuates LYN activity by approximately 80%(5). Correspondingly we decreased the enzymatic activity of LYN in the model to the same extent.

In contrast to the temporal activation dynamics of normal BCR signaling, we imposed constitutive pLYN and pSYK stimulus in simulations of diseased ABC DLBCLs, with negative feedback from SYK and PKC respectively.

$$pLYN = 0.2 * f_{LYN} * T_{LYN}/(100 * pSYK) \quad (9)$$

$$pSYK = f_{SYK} * T_{SYK}/(1 + 100 * PKC) \quad (10)$$

Tℏe 0.2 coefficient is to account for LYN attenuation effect due to CD79B mutation in TMD8. The parameter for negative feedback is estimated by fitting to single drug viability response(43).

To predict cell viability response from signaling output, we formulated a tumor growth model in which the growth rate of tumor cells is dependent on the weighted sum of the three downstream survival and proliferation signals NFκB, ERK and AKT through a Hill function. A similar formalism has been used to characterize tumor growth of

ERBB-amplified breast cancer driven by ERK and AKT activation(45).

Assume a tumor cell population is at exponential growth phase(46, 47),

$$N = N_0 e^{(r-r_d)t} \tag{11}$$

where N_0 and N are cell number at time 0 and time t, r_d is basal death rate, while growth rate r is dependent on three downstream survival and proliferation signals NFκB, pAKT, and pERK (normalized by untreated control) through a Hill function,

$$r = r^* * \frac{(w_1*NF\kappa B+w_2*pAKT+w_3*pERK)^n}{K^n+(w_1*NF\kappa B+w_2*pAKT+w_3*pERK)^n} \tag{12}$$

Here r^* is basal growth rate, n is Hill coefficient, w_1,w_2,w_3 are the estimated weights of three signaling outputs NFκB, pAKT and pERK. Therefore, viability response defined as the ratio of cell number monitored under treated condition N (for a time span of T) and untreated control N_c can be predicted as following,

$$Viability = \frac{N}{N_c} = e^{r^**T(\frac{(w_1*NF\kappa B+w_2*pAKT+w_3*pERK)^n}{K^n+(w_1*NF\kappa B+w_2*pAKT+w_3*pERK)^n}-\frac{(w_1+w_2+w_3)^n}{K^n+(w_1+w_2+w_3)^n})} \tag{13}$$

Parameters required in this function were trained with viability data of three single drug viability responses, namely NFκB, AKT and MEK inhibitor respectively. First the level of the three downstream survival and proliferation signals were predicted via simulation of the signaling model, and then input into the tumor growth functions to compute the viability output. Parameters were chosen by minimizing the sum of residuals between the viability predictions and experimental data.

We used published viability response data in TMD8 to parameterize the tumor growth model, where cells were treated with IKK, AKT and MEK inhibitors at multiple dosages(43). Specifically, using the median effect equation, we calibrated the percent activity left on the targeted kinase for each inhibitor at a given dosage based on the inhibitor's IC_{50} value (**Table 2.3**).

$$\%activity = \frac{1}{1+(\frac{dosage}{IC_{50}})^m} \tag{14}$$

The drug's IC50 was taken from literature(8, 48-58) (**Table 2.3**), while m was assumed to be 1 under a first order approximation. Then the activity of the targeted kinase (i.e. parameters representing catalytic or activation rate of targeted kinase) was reduced to the corresponding percentage in the kinetic model. We list perturbed parameters in each simulated inhibitor treatment in **Table 2.3**.

Table 2.3 Inhibitors against BCR signaling network

Target	Inhibitor	IC_{50}	Perturbed parameter	Reference
LYN	Saracatinib(AZD0530)	5 nM	f_{LYN}	(48)
SYK	PRT060318	4 nM	f_{SYK}	(49)
BTK	Ibrutinib(PCI-32765)	0.5 nM	k_{btk}	(50)
PKCβ	Sotrastaurin(AEB071)	2 nM	k_{pkc}, K_{pkbt}	(51)
MALT1	MI-2	5.84 μM	k_{cbik}	(8)
IKK	NCGC00161703	67 nM	k_{nfkb}	(52)
PI3Kδ	CAL-101	2.5 nM	k_{pi3k}	(53)
	BKM-120	116 nM	k_{pi3k}	(54)
PDK1	BX-795	6 nM	k_{dpak}	(55)
AKT	MK-2206	8 nM	pAKT, K_{akra}	(56)
RAF	CHIR-265	30 nM	k_{rame}	(57)
MEK	Trametinib	0.92 nM	k_{meer}	(58)

We then reduced the activity of the targeted kinase to the same level in the model and simulated steady-state signaling output. Parameters in the tumor growth model were estimated by minimizing residual sum of squares between predicted viability response and experimental data.

We first simulated single drug viability response of inhibitors covering the NFκB, PI3K/AKT and MAPK pathway and compared to experimental data. We observed that *in silico* simulation with the BCR signaling model and the tumor growth model recapitulated the viability response of the three training single drug response, namely IKK, AKT, MEK inhibitors **(Figure 2.8A)**. This is not surprising since the growth model was fitted based on training data. As independent predictions, we also simulated drug response of inhibitors targeting other kinases in the network, e.g. CAL-101 against PI3K, Ibrutinib against BTK, and found that predicted viability response matched favorably with TMD8 drug response data **(Figure 2.8B)**. At the same time, we found simulated viability response of SYK inhibition to deviate from experimental data (grey line), yet this discrepancy can be partially rescued by adding a negative feedback from SYK to LYN (blue line). It has been reported that SYK functions as a negative regulator of BCR signaling by phosphorylating Ig-α. Since Ig-α primarily interacts with LYN, we assumed in the model that SYK indirectly negatively regulates LYN.

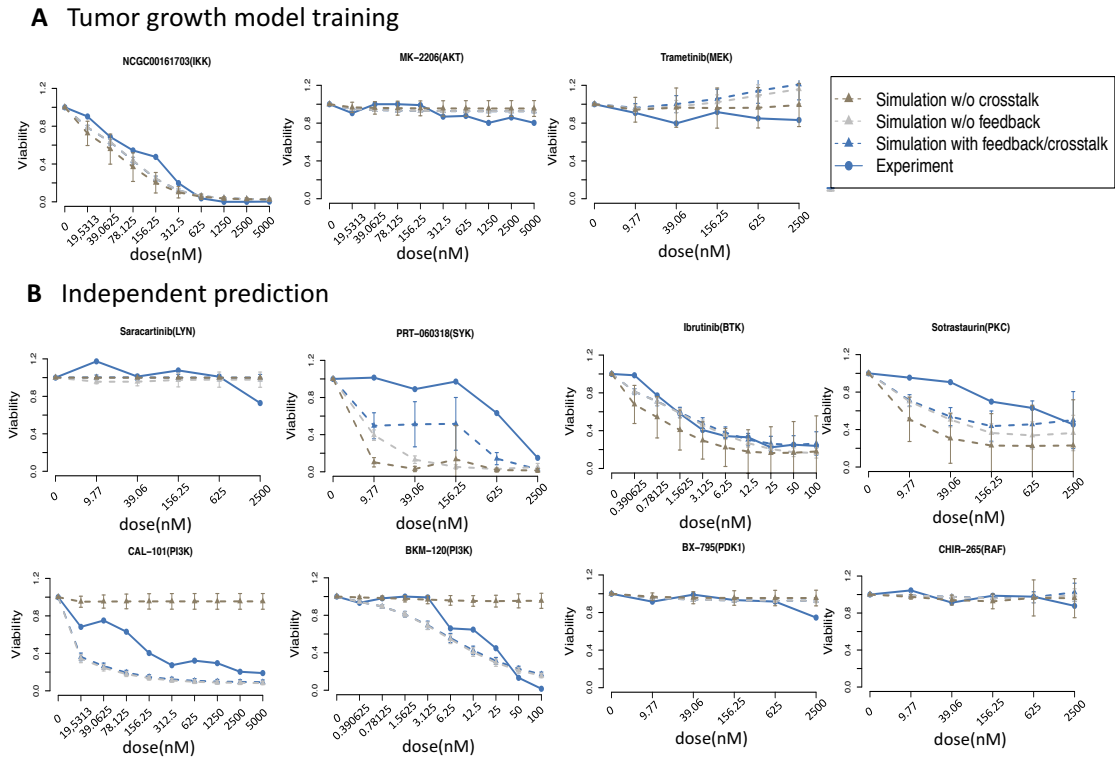

Figure 2.8 Training and prediction of single drug viability response in ABC DLBCL cell line TMD8. (**A**) Tumor growth model parameterization using single drug viability response of inhibitors targeting NFκB, AKT and MEK. Gray dashed lines correspond to simulation results of model without SYK to LYN negative feedback, while brown dashed lines correspond to simulation results of model without PI3K-NFκB crosstalk. (**B**) Single drug viability response of inhibitor targeting various kinases against BCR signaling network.

Beyond single drug viability response, we also simulated combinatorial drug response of Ibrutinib in combination with various other kinases targeting the BCR pathway, and observed the predicted response contour to match favorably with experimental results

(Figure 2.9). These results demonstrate that our model can correctly capture the interaction between inhibitors as well.

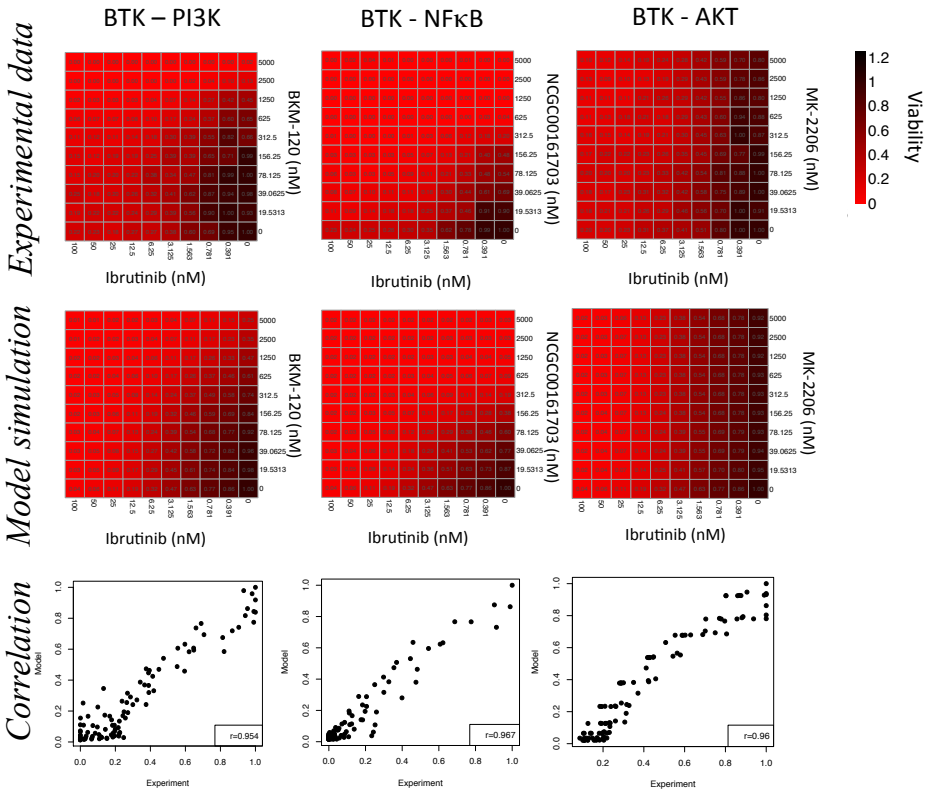

Figure 2.9 Combinatorial drug viability responses of BTK inhibitor Ibrutinib in combination with additional inhibitors targeting BCR network intermediates were predicted and compared with experimental data.

Overall, these results suggest that viability response of small molecule inhibitors targeting the BCR signaling network can be predicted via *in silico* simulation of the BCR signaling model in combination with the tumor growth model.

2.3 Crosstalk between PI3K and NFκB pathway mediates efficacy of PI3K inhibition in TMD8

In both the drug response data and model's simulation, we observed that PI3K inhibition is significantly more effective at inhibiting tumor growth than blockage of its downstream effector AKT. A similar phenomenon was reported in other studies, where PI3K inhibition was shown to attenuate NFκB transcriptional activity(6, 59). We hypothesized that the efficacy of PI3K inhibition is primarily attributed to suppression of NFκB signaling, which is mediated by upstream crosstalk between the PI3K and NFκB pathways. To test this hypothesis, we abolished the crosstalk between PI3K and NFκB by knocking out *in silico* $PI(3,4,5)P_3$ -mediated membrane recruitment of BTK in the signaling model. Under this condition we re-simulated the viability response of PI3K inhibition, which showed significant reduction compared to both experimental data and simulation with the full signaling model **(Figure 2.8, brown line)**. This result supports the notion that the upstream crosstalk between PI3K and NFκB pathway is critical in mediating tumor growth inhibition by PI3K inhibitor. It also provides further rational support for the clinical use of PI3K inhibitors in DLBCL that are dependent in NFκB signaling(6, 59).

2.4 Computational optimization of targeted therapy against chronic active BCR signaling

Using the above modeling framework, we sought to identify targeted therapies against the BCR signaling network that most effectively inhibit tumor growth. We exhaustively tested all drug pairs based on 11 small molecule inhibitors currently available that target various kinases in the network, yielding 55 treatment strategies in total. In each scenario viability response was simulated at 10 by 10 virtual dosages where each targeted kinase was inhibited at 0% to 99% evenly spaced in log10 space. We calculated area under the combinatorial viability response surface as an overall indicator of drug combination potency. The smaller the value is, the more potent the drug target combination is (**Figure 2.10A**). We found that under the same inhibition potency, efficacy of different treatment strategies was highly variable, ranging from almost no growth inhibition to up to 80% reduction (**Figure 2.10B**). Specifically, inhibiting downstream of the NFκB signaling pathway, especially through MALT1 and IKK inhibitor, exhibited the most prominent efficacy, and combined MALT1 and IKK blockage yielded highest tumor growth inhibition. In comparison, tumor cell growth was relatively insensitive to blockage of MAPK pathway in our simulations. In summary, this computational screening result suggests that various treatment strategies against a signaling network can yield highly variable therapeutic responses and that in *silico* simulation can help identify targets that confer intrinsic vulnerability.

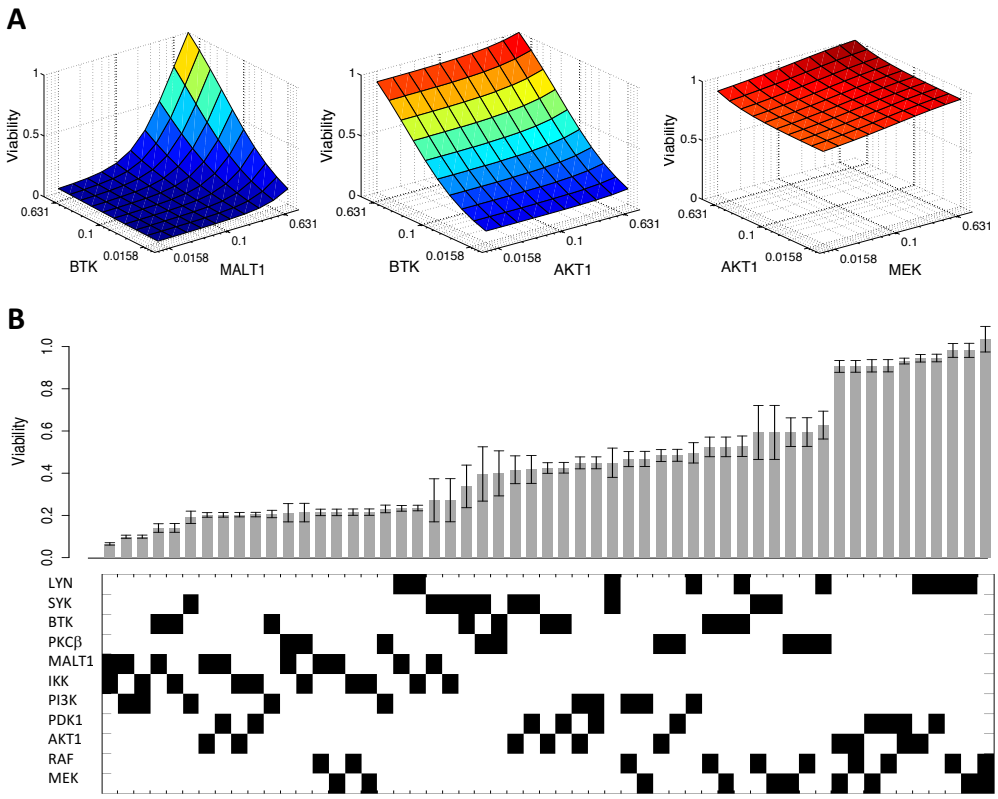

Figure 2.10 Computational optimization of treatment strategy against chronic active BCR signaling (**A**) Viability response surface of three drug target combinations. Two horizontal axis corresponds to virtual dosage of two different inhibitors while the vertical axis indicates cell viability normalized to untreated condition. For each drug target combination, 10 virtual dosages (between 0% to 99% inhibition evenly spaced in log10 space) of each single drug are tested. (**B**) Barplot of simulated viability response of all possible dual inhibition on 11 kinases in the BCR signaling network that are currently targetable. Here viability responses are calculated area under the combinatorial viability response surface (as shown in Fig 6A) as an overall indicator of drug combination potency. Binary codes on the bottom indicate the treatments applied (black represents targeted inhibition).

We then sought to identify drug combinations that are synergistic via computational simulations. For a given two-drug combination, the combinatorial drug response at 10 by 10 virtual dosage as discussed above were used to estimate mode of drug interaction under the Bliss independence model.

Under the Bliss Independence model, the additive effect of two inhibitors is computed as the multiplication of the effect of individual inhibitors,

$$F_{UA} = F_{UA_1} * F_{UA_2} \tag{15}$$

where F_{UA} indicates the fraction unaffected. To evaluate mode of interaction between two inhibitors, we computed viability response at 10x10 virtual dosages by varying the percent inhibition of each targeted kinase independently from 0% to 90% at 10% interval. These viability values were used to estimate parameter that minimizes the following metric,

$$\sum(F_{UA_{1x2y}} - \beta * F_{UA_{1x}} * F_{UA_{2y}})^2 \tag{16}$$

where x,y are virtual dosages for inhibitor 1 and 2 respectively. $\beta < 1, \beta = 1, \beta > 1$ indicates synergism, additive and antagonism respectively.

Computational screening predicted dual blockage of LYN and SYK as the most synergistic combination**(Figure 2.11A)**. To test this prediction, we treated ABC DLBCL cell lines TMD8, HBL1 and OCI-LY10 with LYN inhibitor Dasatinib and SYK inhibitor R406, at multiple doses. Comparing combinatorial drug response data to theoretical additive response predicted by the Bliss independence model, we confirmed synergism between Dasatinib and R406 (**Figure 2.11B**). We also tested and confirmed the predicted antagonism between dual SYK and MALT1 inhibition using SYK inhibitor R406 and MALT1 inhibitor MI-2 across three ABC DLBCL cell lines (**Figure 2.11B**).

Figure 2.11. Prediction and validation of synergistic and antagonistic drug combinations. (**A**) Modes of interaction of all pairwise inhibitions under Bliss Independence model. $\beta<1$, $\beta=1$, $\beta>1$ correspond to synergism, additive and antagonism respectively. (**B**) In vitro validation of predicted synergistic and antagonistic drug combination in ABC DLBCL cell line TMD8, HBL1 and OCI-LY10. R406, Dasatinib and MI-2 are inhibitors against SYK, LYN and MALT1 respectively.

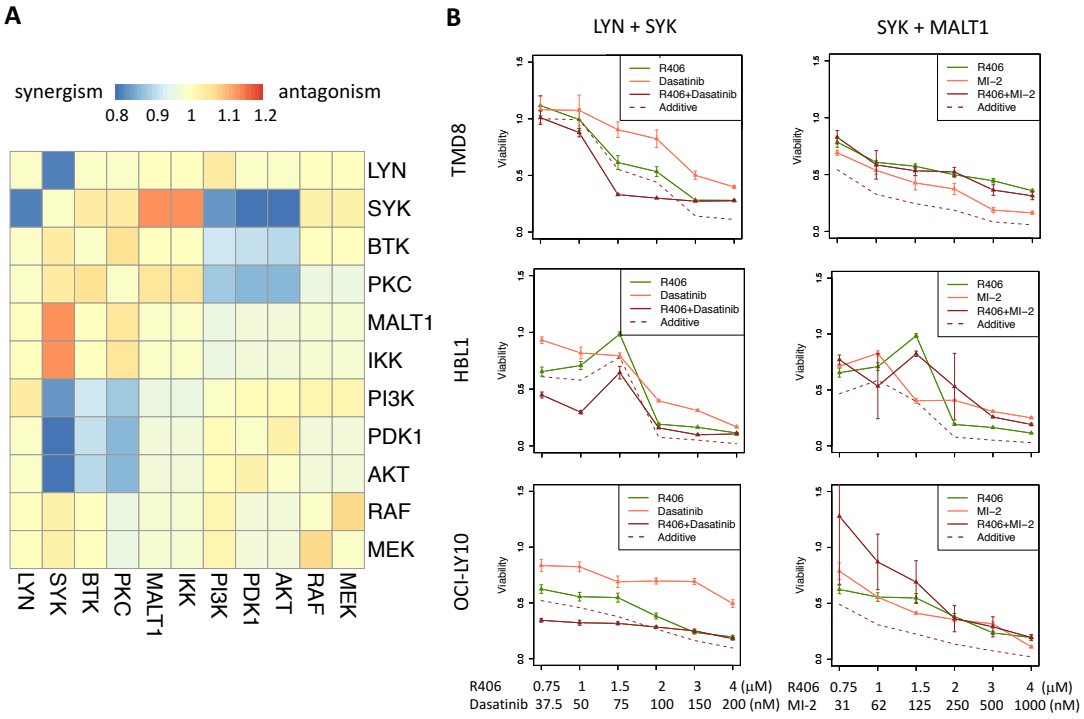
A
synergism
antagonism
0.8 0.9 1 1.1 1.2
LYN
SYK
BTK
PKC
MALT1
IKK
PI3K
PDK1
AKT
RAF
MEK
B
LYN + SYK
SYK + MALT1
TMD8
HBL1
OCI-LY10
Viability
R406
Dasatinib
R406+Dasatinib
Additive
MI−2
R406+MI−2
R406 0.75 1 1.5 2 3 4 (μM)
Dasatinib 37.5 50 75 100 150 200 (nM)
R406 0.75 1 1.5 2 3 4 (μM)
MI-2 31 62 125 250 500 1000 (nM)

2.5 Comparison of the kinetic model to a simpler Boolean network model

In this work, we choose to develop a highly detailed kinetic model of the BCR signaling network, modeling direct protein-protein interactions using highly quantitative ODEs wherever possible. We note that there are other simpler modeling techniques for analysis of signaling pathways, e.g. simplifying signaling cascades as coupled Hill functions(45) or using Boolean network models. To investigate the predictive power of a simpler model, we constructed a Boolean model of a simplified BCR signaling network consisting of only the 11 targetable nodes together with signaling pathway end points and a node representing cell viability (**Figure 2.12**).

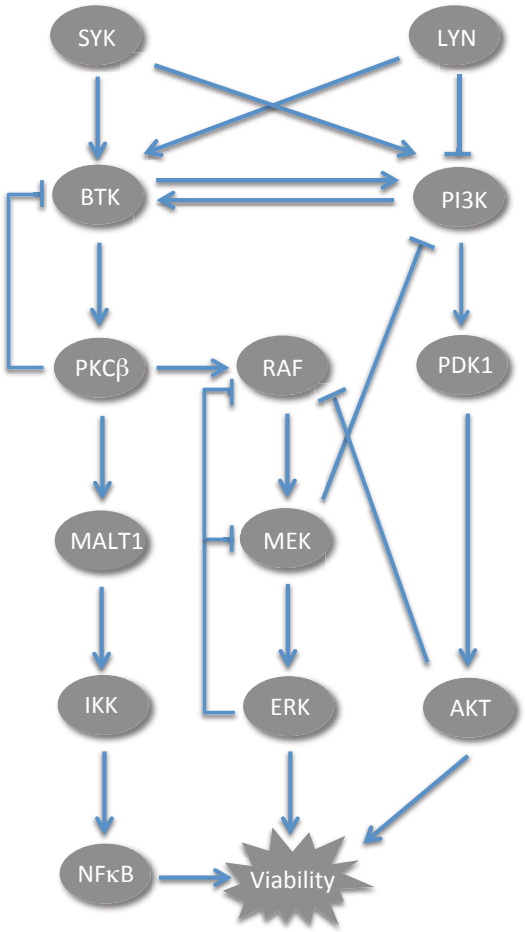

Figure 2.12. Simplified BCR signaling network consisting of only the 11 targetable nodes together with signaling pathway end points and a node representing cell viability.

In this model, each node has only two states (0-inactive and 1-active), and the state value in a particular step is determined by the values of all its regulators in the previous step. A node will be active if the majority of its regulators are activating, except that the Viability node is active when any of the signaling outputs is active. Assuming the two input nodes LYN and SYK are constitutively active, all possible initial states (2^12) are

exhaustively simulated until reaching attractors. These initial states ended up in two attractors, both attractors consisting of states in which Viability is on (**Figure 2.13**).

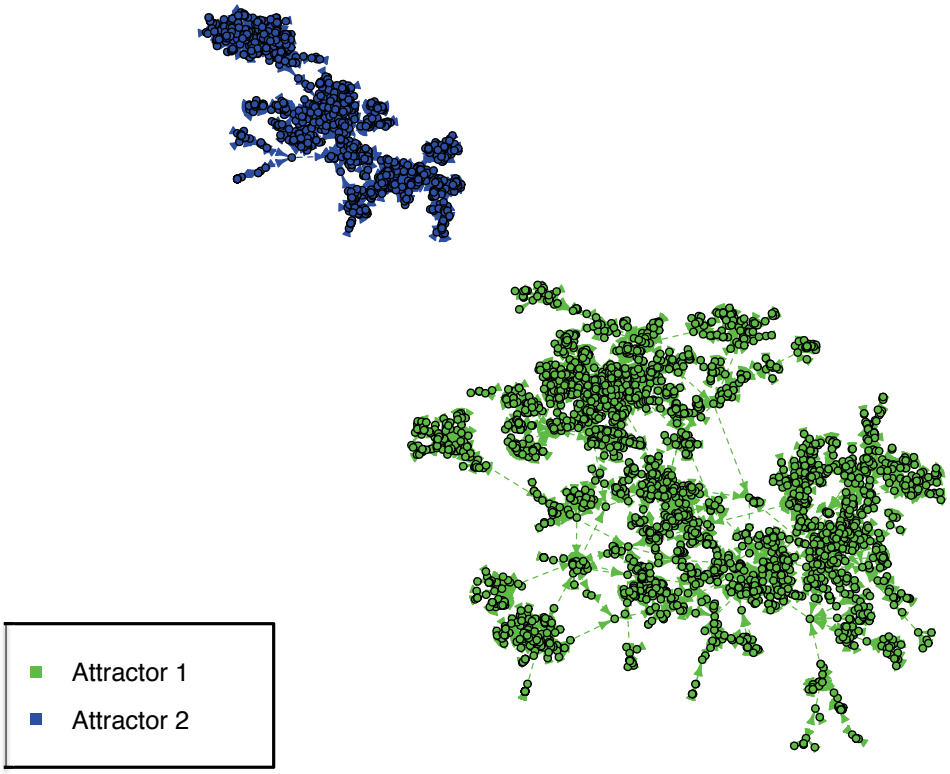

Figure 2.13 Attractor landscape of Boolean network model.

Then all two drug combinations were tested. To simulate drug-mediated inhibition, each targeted node was made constitutively inactive. There are four drug combinations that result in a single global attractor in which Viability is off. These four drug combinations are BTK-MEK, BTK-RAF, SYK-MEK, SYK-RAF. These four drug combinations ranked low in the drug efficacy predictions made by the full ODE model (**Figure 2.10B**). Moreover, experimental data in TMD8 cell line(43) indicates that the

BTK-MEK and BTK-RAF combinations are not very effective in decreasing cell viability – the MEK and RAF inhibitors are not responsive (along the y axis) and synergism is lacking (**Figure 2.14**).

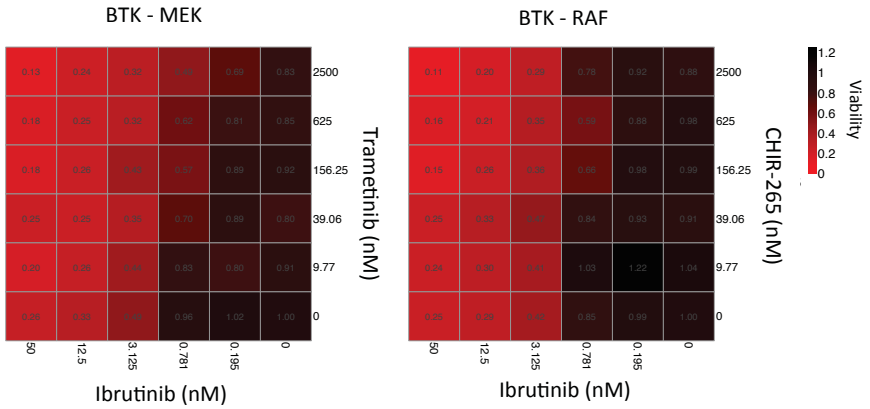

Figure 2.14 Viability response of drug combination BTK+MEK and BTK+RAF in TMD8. Ibrutinib, Trametinib and CHIR-265 are inhibitors of BTK, MEK and RAF respectively.

Overall, these results suggest that a simple Boolean network model is not able to capture the same results as the full ODE model and that its prediction accuracy is lacking when compared to experimental data.

CHAPTER THREE

PREDICTING ABC VS. GCB SUBTYPES OF DIFFUSE LARGE B CELL LYMPHOMA FROM RNA-SEQ DATA

3.1 Z score normalization and Bayesian classifier for ABC/GCB DLBCL classification

We use the microarray dataset from Lenz et al.(60) as training data, which has predetermined ABC/GCB classification labels. With the goal of being able to classify datasets from different platforms, we first apply z score standardization to both training and the to-be-classified data, where we center and scale each gene across all samples and then perform log transformation to make the data more normally distributed (**Figure 3.1**). This procedure puts the two datasets into comparable scale and distribution. Then we select the top N (default to 50) most differentially expressed genes ranked by p value between the ABC and GCB groups in the training data as determined by student's t-test as genes in the Bayesian predictor. A linear predictor score(LPS) for each sample in the training and to-be-classified data is then calculated,

$$LPS(X) = \sum_{j=1}^{50} a_j X_j$$

where X_j is the expression level of j th gene in the predictor and a_j is the t statistic of j th gene in the t test. Then we calculate the likelihood that a sample is in each of the two subgroups by applying Bayes'rule:

$$P(X\ in\ group\ 1) = \frac{\phi(\mathrm{LPS(X)}; \hat{\mu}_1, \hat{\sigma}_1^2)}{\phi(\mathrm{LPS(X)}; \hat{\mu}_1, \hat{\sigma}_1^2) + \phi(\mathrm{LPS(X)}; \hat{\mu}_2, \hat{\sigma}_2^2)}$$

where $\phi(\mathrm{LPS(X)}; \hat{\mu}, \hat{\sigma}^2)$ represents the normal density function given mean $\hat{\mu}$ and variance $\hat{\sigma}^2$ estimated from a training set subgroup. We set 90% certainty as cutoff for subgroup assignment.

Figure 3.1 Diagram of the approach taken in the study. First z score standardization following log transformation is performed in both training and to-be-classified data respectively. Then top 50 most differentially expressed genes between ABC and GCB groups are determined by student's t-test in the training data set. These 50 genes are used to form a linear predictor. Samples are then classified into ABC vs. GCB groups according to Bayes'rule.

Log transform of Z-score standardization on training and to-be-classified data respectively

Training data

	Sample 1	…	Sample N
Gene 1			
…			
Gene M			

To-be-classified data

	Sample 1	…	Sample N
Gene 1			
…			
Gene M			

Student's t test to determine the top N most differentially expressed genes in the predictor

Calculate Linear Predictor Score(LPS) for each sample in the training and to-be-classified data

$$LPS(X) = \sum_{j=1}^{N} a_j X_j$$

Calculate the likelihood that a sample is in each of the two subgroups by applying Bayes' rule

$$P(X\ in\ group1) = \frac{\phi(LPS(X); \hat{\mu}_1, \hat{\sigma}_1^2)}{\phi\left(LPS(X); \hat{\mu}_1, \hat{\sigma}_1^2\right) + \phi(LPS(X); \hat{\mu}_2, \hat{\sigma}_2^2)}$$

3.2 Testing the ABC/GCB classifier within the pre-labeled microarray dataset

To test the performance of the ABC/GCB classifier, we randomly equally divided the pre-labeled microarray dataset into a training (37 ABCs, 36 GCBs) and a validation set (37 ABCs, 35 GCBs). We then performed student's t-test on the training set to determine 50 top differentially expressed genes between ABC/GCB as predictors. Then we calculated the LPS for each sample and applied Bayes' rule to each sample to assign a label(ABC, GCB or unclassified). Then we compared model-derived classification to existing labels (**Figure 3.2**). The overall consistency was 100% in the training set and 93.1% in the validation set. Similar consistency was achieved when the top 25 (97.3% in the training set and 93.1% in the validation set) or top 100 (97.3% in the training set and 90.3% in the validation set) differentially expressed genes were selected instead of top 50.

Figure 3.2 Classification on microarray dataset and comparison to pre-existing labels. ClassifiedLabel corresponds to Bayesian classifier predicted subtype while Subtype corresponds to pre-labeled subtype **(A)** Classification of training set. **(B)** Classification of validation set.

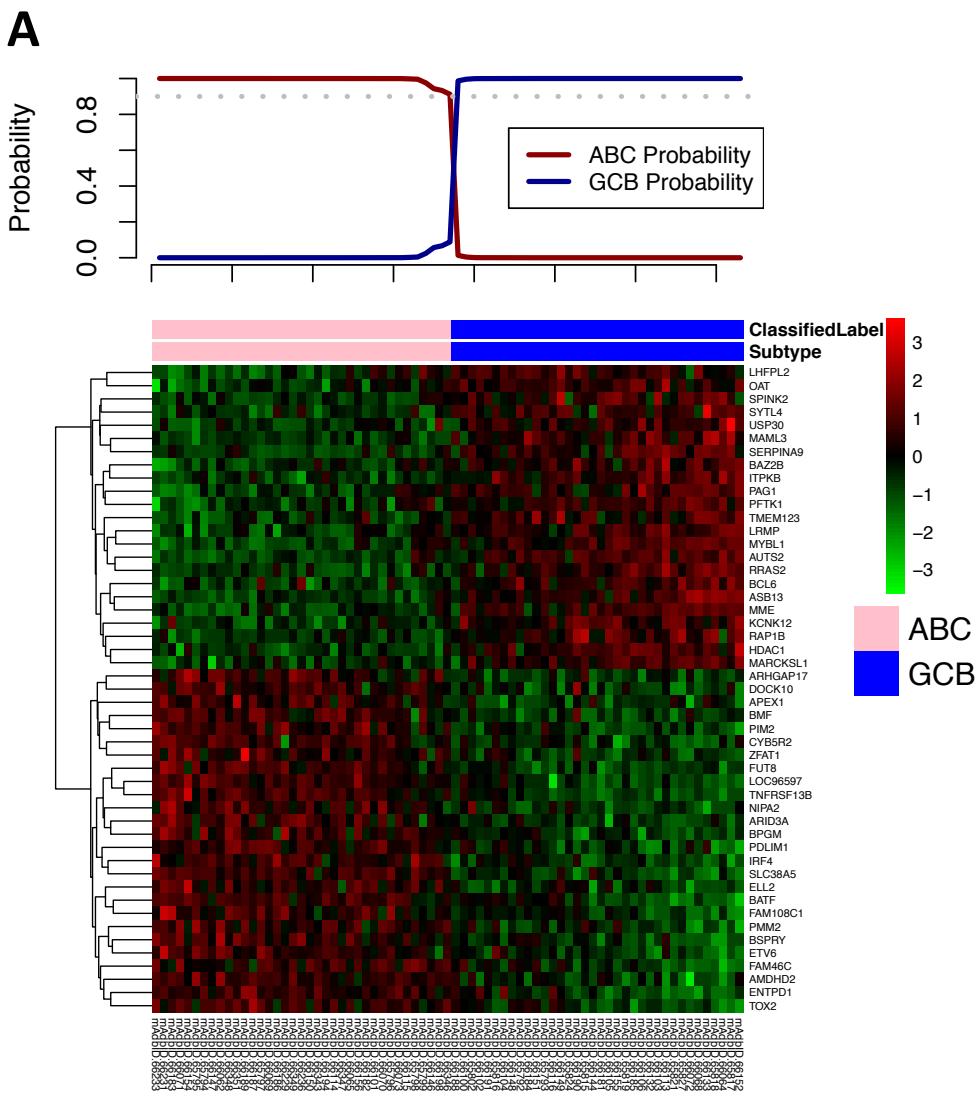
A
Probability
0.0
0.4
0.8
ABC Probability
GCB Probability
ClassifiedLabel
Subtype
LHFPL2
OAT
SPINK2
SYTL4
USP30
MAML3
SERPINA9
BAZ2B
ITPKB
PAG1
PFTK1
TMEM123
LRMP
MYBL1
AUTS2
RRAS2
BCL6
ASB13
MME
KCNK12
RAP1B
HDAC1
MARCKSL1
ARHGAP17
DOCK10
APEX1
BMF
PIM2
CYB5R2
ZFAT1
FUT8
LOC96597
TNFRSF13B
NIPA2
ARID3A
BPGM
PDLIM1
IRF4
SLC38A5
ELL2
BATF
FAM108C1
PMM2
BSPRY
ETV6
FAM46C
AMDHD2
ENTPD1
TOX2
3
2
1
0
−1
−2
−3
ABC
GCB

(Continued Figure 3.2)

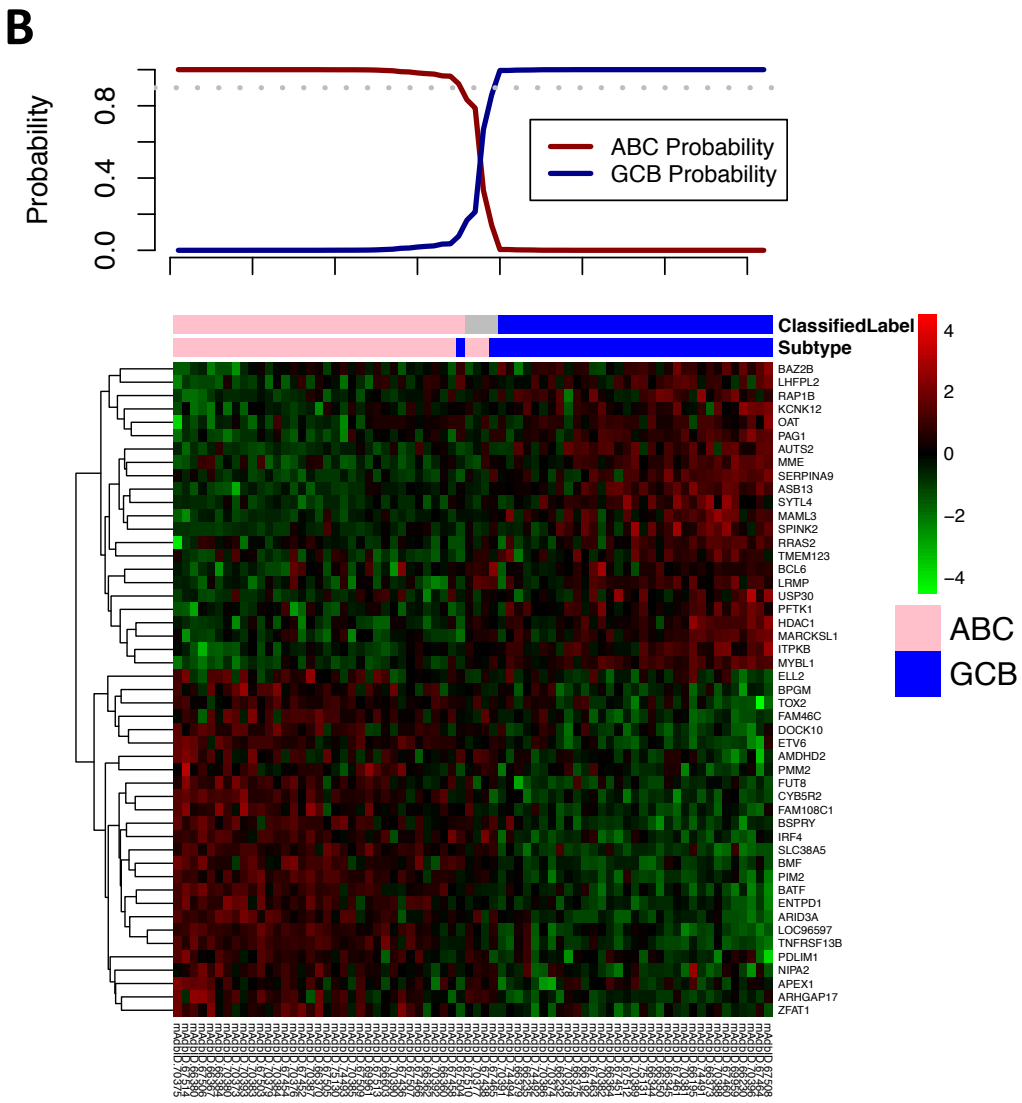

3.3 Applying ABC/GCB classifier to clinic cohort and comparison with IHC label and Lymph2Cx 20 gene signature profiling.

We then sought to test the ABC/GCB classifier on an RNA-Seq dataset by applying it to a cohort consisting of 68 DLBCL patients. Upon alignment using STAR(61), FPKM values of RNA-Seq profiles were calculated using Cufflinks(62) with default parameters. Within the top 50 most differentially expressed genes in the labeled microarray dataset, 45 genes are present in the RNA-Seq dataset. We therefore used these 45 genes as genes in the predictor to classify ABC and GCB subtypes. To maximize predictive power, all microarray data with ABC/GCB label was used for training. Out of the 68 DLBCL patient samples, 30 were classified as ABC and 30 were classified as GCB, with a remaining 8 being unclassified.

We first compared the RNA-Seq based ABC/GCB classification to immunohistochemistry (IHC) labels. The overall consistency is 46.4%(**Figure 3.3**). By randomly permuting both the RNA-Seq based classification labels and IHC labels 10,000 times, we determined that this consistency is not statistically significant ($p=0.234$).

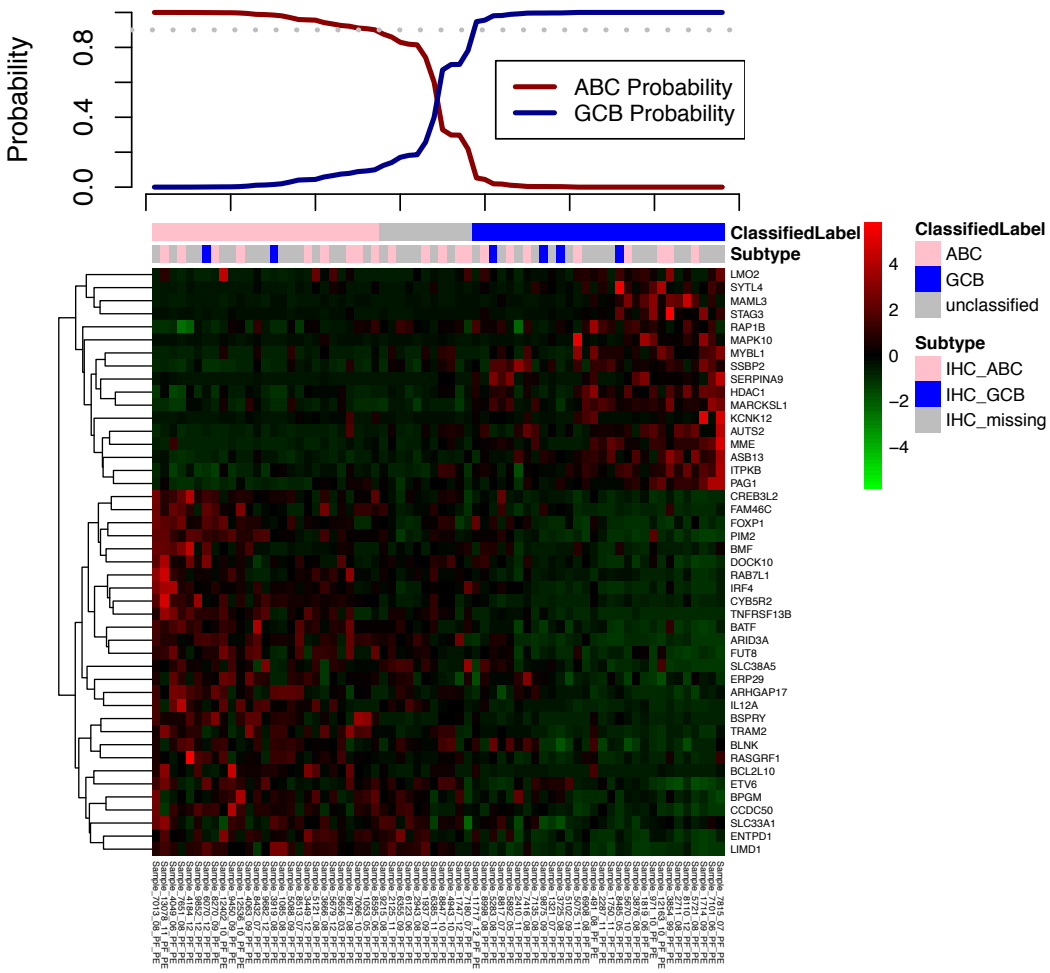

Figure 3.3 Classification of RNA-Seq data and comparison to IHC labels. ClassifiedLabel corresponds to Bayesian classifier predicted subtype while Subtype corresponds to IHC determined subtype.

We then compared our classification to Lymph2Cx 20 gene signature profiling(63). This 20 gene signature consists of 8 genes being overexpressed in ABC DLBCLs, 5 house-keeping genes, and 7 genes being overexpressed in GCB DLBCLs. We applied

hierarchical clustering to the centered and scaled 20 gene expression signature RNA-Seq data (**Figure 3.4A**). The result demonstrates good consistency with our classification, where ABC or GCB samples are largely clustered independently. This is not surprising as we note that most of the genes included in the Lymph2Cx 20 gene signature (excluding the 5 house-keeping genes) are present in our classifier(**Figure 3.4B**).

Figure 3.4 Hierarchical clustering based on Lymph2Cx 20 gene signature profiling and comparison between genes in Bayesian classifier and in Lymph2Cx 20 gene signature. **(A)** Hierarchical clustering based on Lymph2Cx 20 gene signature profiling. **(B)** Venn diagram showing overlap between genes in RNA-Seq Bayesian classifier and Lymph2Cx 20 gene signature. Blue corresponds to RNA-Seq Bayesian classifier while pink corresponds to Lymph2Cx 20 gene signature.

A

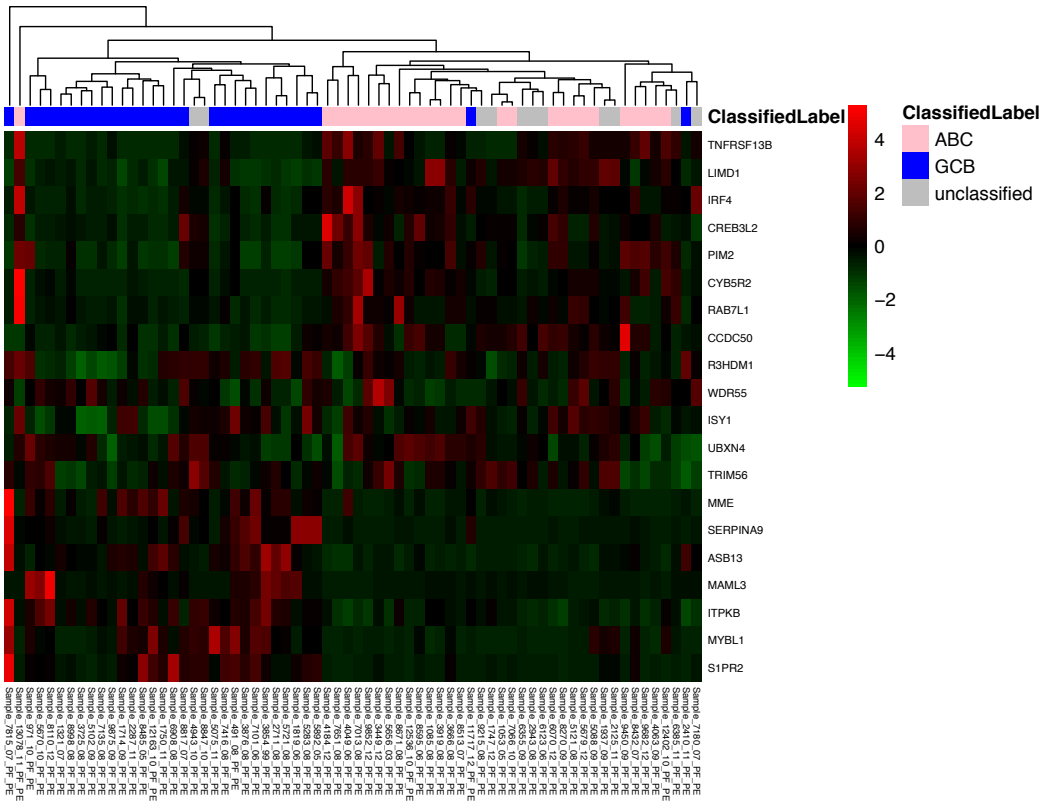
ClassifiedLabel
TNFRSF13B
LIMD1
IRF4
CREB3L2
PIM2
CYB5R2
RAB7L1
CCDC50
R3HDM1
WDR55
ISY1
UBXN4
TRIM56
MME
SERPINA9
ASB13
MAML3
ITPKB
MYBL1
S1PR2
ClassifiedLabel
4
2
0
−2
−4
ClassifiedLabel
ABC
GCB
unclassified

(Continued Figure 3.4)

B

Up in ABC

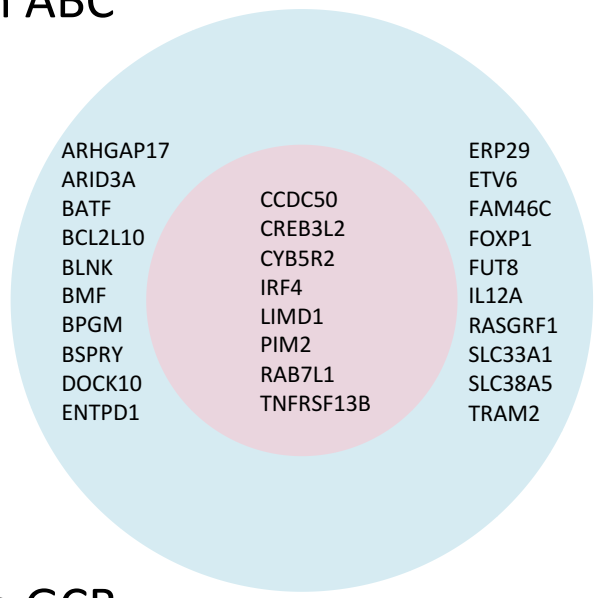

Up in GCB

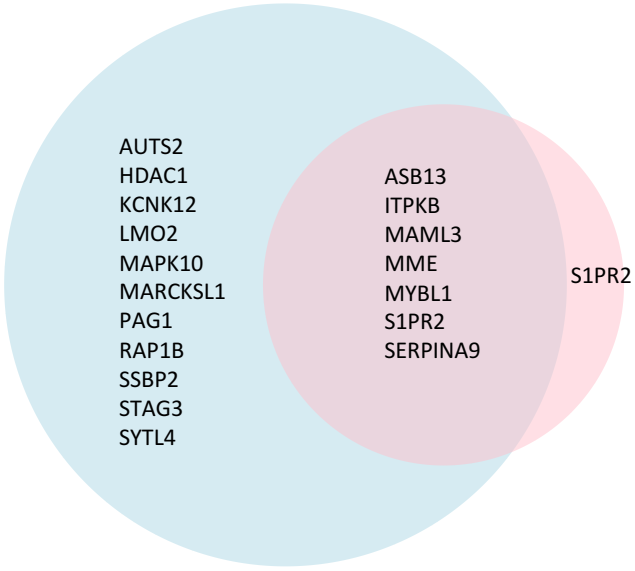

3.4 RNA-Seq based ABC/GCB classifier outperformed IHC label in stratifying two subgroups with distinct probability of survival.

Since the consistency between RNA-Seq based ABC/GCB classification and IHC-based labeling is low, we sought to compare how each classification associates with survival probability. Using Kaplan-Meier plots, we found that the IHC-based labeling is not able to stratify two groups with distinct survival probability while the RNA-Seq based classification succeeded (**Figure 3.5**). P values were determined using a one variable Cox model and confirmed the results shown in the Kaplan-Meier plots. We also investigated the performance of a Bayesian classifier built on genes in the Lymph2Cx profiling. For this classifier, 14 genes that discriminate between ABC and GCB subtype (excluding the 5 house keeping genes) and are present in both the microarray training data and RNA-Seq data are used to construct the predictor. We found that classification based on these 14 genes gave less significant survival stratification probability compared to our classifier (**Figure 3.5**).

Figure 3.5 Kaplan-Meier plots of patient survival in subgroups defined by IHC labels or RNA-Seq classification. P values were determined by one variable Cox model. **(A)** Two groups represent IHC labeled ABC or GCB subtype. **(B)** Two groups represent ABC or GCB classification based on our RNA-Seq Bayesian classifier **(C)** Two groups represent ABC or GCB classification based on RNA-Seq Bayesian classifier with Lymph2Cx genes.

A

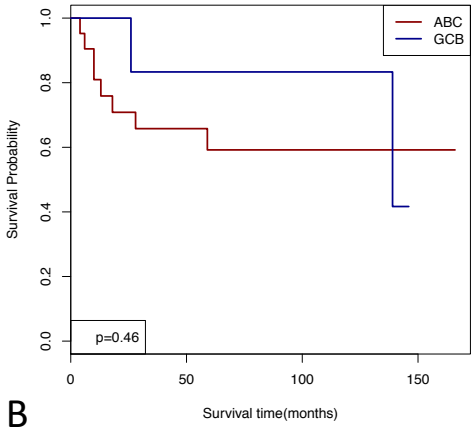
ABC
GCB
Survival Probability
0.0
0.2
0.4
0.6
0.8
1.0
p=0.46
0
50
100
150
Survival time(months)

B

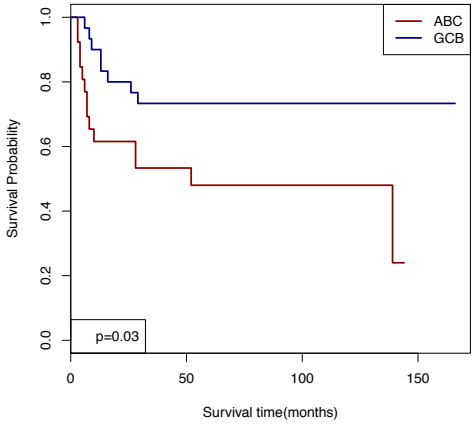
ABC
GCB
Survival Probability
0.0
0.2
0.4
0.6
0.8
1.0
p=0.03
0
50
100
150
Survival time(months)

C

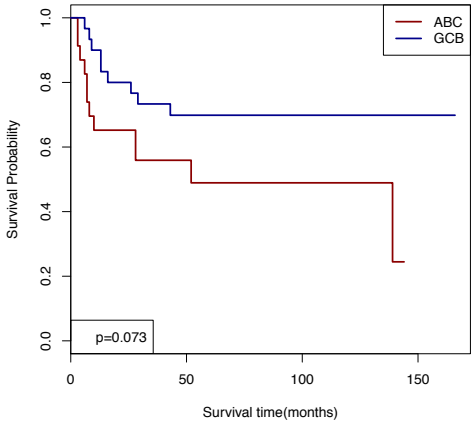
ABC
GCB
Survival Probability
0.0
0.2
0.4
0.6
0.8
1.0
p=0.073
0
50
100
150
Survival time(months)

CHAPTER FOUR DISCUSSION

It is increasingly acknowledged that aberrant BCR signaling plays a central role in the development and maintenance of many B cell malignancies(64). Though a large panel of small molecule inhibitors against BCR signaling have been developed, rational methodologies that can predict effective combinatorial therapy and guide the design of specific treatment strategy in individual patients have been lacking. To bridge this gap, we aimed to construct the first kinetic model of the core BCR signaling network and use this model to investigate targeted therapy against BCR signaling. We showed that simulations with the signaling model reconstructed dynamics of normal B cell signaling *in silico*. Combining the signaling model with a data-trained tumor growth model successfully predicted viability response of multiple drug combinations, and identified novel synergistic drug combinations such as LYN and SYK inhibitor.

As one of the most important signaling event in B cells, antigen triggered BCR activation has been intensively studied during the past decades. Detailed molecular interactions in the key signal transduction pathway as well as regulatory feedback loops were experimentally identified, providing a unique opportunity to establish a detailed kinetic model of the BCR signaling network. Prompted by the rich information available in literature, we attempted to establish the first kinetic model to quantitatively characterize BCR signaling *in silico*. The model is able to reproduce major kinetic features of BCR signaling observed in experiments. However, we note that simplifications and assumptions in the model may call for further improvements. First

of all, how antigen recognition leads to proximal BCR activation, namely phosphorylation of BCR ITAM motif, LYN and SYK, was not addressed in the model. Integration of proximal BCR signaling with downstream signaling model characterized here can potentially provide a more comprehensive understanding of how different strengths of antigen stimulus might lead to various downstream effector activation and distinct cell fate decision. Critically, a negative feedback loop between downstream Ca^{2+} response and upstream phosphatase activity mediated by reactive oxygen species (ROS) may play an important role in determining the threshold and amplitude of BCR response(65). Furthermore, we did not account for transcriptional regulation of key elements in the BCR signaling network that may influence long term signaling response. Expression of BLNK, CD79A, SYK, BTK, and CD19 is transcriptionally repressed by BLIMP-1, which is activated during germinal center to plasma B cell differentiation triggered by BCR activation(66). Additionally, chemical inhibition of SYK was shown to induce compensatory upregulation of SYK expression mediated by FOXO1(6). Thus, these transcriptional feedbacks that attempt to upregulate expression of components in the BCR signaling network upon signaling attenuation may mediate resistance to BCR-targeted therapy to some extent.

Oncogenic activation of intracellular signaling pathways drives tumor survival and proliferation by engaging regulators that antagonize apoptosis or drive cell cycle progression. In the BCR signaling network, NFκB transcribes anti-apoptotic factors such as BCL2 and BCR-xL(67) and cell cycle regulators such as cyclin D2(68). Conversely, AKT and ERK indirectly repress pro-apoptotic factors, e.g., BIM and BAD

as well as negative regulators of CDKs such as $p27^{kip1}$ and $p21^{cip1}$(69, 70). A mechanistic characterization of how NFκB, AKT and ERK signal influences tumor survival and proliferation requires deep quantitative knowledge of apoptosis and cell cycle regulation. In this model, we addressed this question by parameterizing a phenotypic tumor growth model from drug response data in TMD8. This parameterization revealed TMD8 to be primarily dependent on NFκB signaling. Under this condition, dual inhibition of IKK and MALT1, two major kinases in the downstream of NFκB signaling cascade, was predicted to have highest growth inhibition efficacy. However, we note that the dependency of various survival and proliferation signals may vary from patient to patient and even dynamically evolve as tumors develop. Indeed, some GCB subtype DLBCL cell lines have been shown to be more sensitive to AKT and ERK inhibition than ABC DLBCLs(71, 72). When one pathway is blocked by targeted therapy, tumors may adapt by utilizing alternative pathways that remain constitutively active. Consequently, simultaneous repression of all oncogenic pathways, e.g., through dual inhibition of BTK and PI3K, or sequential administration of agents targeting various pathways may ensure more durable response. Monitoring tumor growth and probing signaling dependency for longer periods would help establish mathematical models that can optimize for long-term benefits.

The clinical application of targeted therapy is frequently challenged by highly variable drug response among cancer patients. Heterogeneous response to BCR signaling-targeted therapy was observed in ABC DLBCL cell lines(59) and in clinical trials of

ABC DLBCL patients(10). This is likely due to differential expression of proteins in the BCR signaling pathway that impact pathway activities in individual patient. In our present study, signal transduction is explicitly modeled on the molecular level, which provides a straightforward framework to incorporate protein level variation to develop patient-specific predictive models. Specifically, expression levels of proteins within the BCR signaling network can be measured experimentally using protein expression profiling techniques such as Reverse Phase Protein Array (RPPA) or other approaches. Then protein expression changes in patients relative to cell line can be incorporated into the model to predict optimal treatment strategy for individual patients. We believe that the use of patient-specific predictive models can greatly improve the performance of targeted therapy in cancer.

We note that besides DLBCL, aberrant BCR signaling was shown to play a role in other B cell malignancies such as chronic lymphocytic leukemia (CLL)(73) and mantle cell lymphoma(MCL)(74). In Phase II studies of BTK inhibitor Ibrutinib, 71% and 68% overall response rate (ORR) was reported in CLL and MCL patients respectively, suggesting targeting BCR signaling as promising treatment strategy. Correspondingly, the overall framework and predictions reported in this work may also be useful to identify drug combinations for CLL and MCL targeted treatment.

With a number of advantages of RNA-Seq technology over microarray, i.e. the ability to discover novel transcripts, RNA-Seq technology is increasingly used for gene expression profiling in cancer studies. While the importance of gene expression based stratification of DLBCL subtypes is widely appreciated, all published methods are based on microarray platform and application to RNA-Seq data is lacking. To bridge this gap, we adapted the original Bayesian classifier method(4) and demonstrate generalizability to RNA-Seq data upon log transformation of z score standardization of both training and to-be-classified data. By randomly equally splitting the pre-labeled microarray dataset into a training and validation set, we demonstrated that our method performed well on the original microarray dataset. Furthermore, we applied our method to a primary DLBCL RNA-Seq dataset. While our classification of ABC and GCB subtypes showed good consistency with the hierarchical clustering result of Lymph2Cx 20 gene signature, it matched poorly with IHC labels. However, we further demonstrated that the RNA-Seq based ABC/GCB stratification significantly outperformed the IHC label in stratifying two subgroups with distinct probability of survival.

A key step in generalizing the classification method to RNA-Seq data is to perform z-score normalization on both training and to-be-classified data. This step puts the training microarray dataset and the to-be-classified RNA-Seq data on the same scale. However it is important to note that we now utilize the relative expression across samples as input for classification instead of absolute expression values. In other words, we leverage the fact that within a clinical cohort of DLBCLs there would naturally be a subset of ABCs and a subset of GCBs, and the relative gene expression differences

between the ABC and GCB subsets should be able to stratify between these two groups. A concomitant issue is that when the to-be-classified dataset has very small number of samples, the classification can become inaccurate as the samples are likely to be highly unevenly distributed between ABC and GCB, i.e. all be ABCs or GCBs. In this case to increase classification accuracy it would be important to put the few to-be-classified cases with other available DLBCL samples to form a larger cohort and to perform classification once on this larger cohort.

References

1. Du W, Elemento O. Cancer systems biology: embracing complexity to develop better anticancer therapeutic strategies. Oncogene. 2015;34(25):3215-25.

2. Rosenwald A, Wright G, Chan WC, Connors JM, Campo E, Fisher RI, et al. The use of molecular profiling to predict survival after chemotherapy for diffuse large-B-cell lymphoma. N Engl J Med. 2002;346(25):1937-47.

3. Alizadeh AA, Eisen MB, Davis RE, Ma C, Lossos IS, Rosenwald A, et al. Distinct types of diffuse large B-cell lymphoma identified by gene expression profiling. Nature. 2000;403(6769):503-11.

4. Wright G, Tan B, Rosenwald A, Hurt EH, Wiestner A, Staudt LM. A gene expression-based method to diagnose clinically distinct subgroups of diffuse large B cell lymphoma. Proc Natl Acad Sci U S A. 2003;100(17):9991-6.

5. Davis RE, Ngo VN, Lenz G, Tolar P, Young RM, Romesser PB, et al. Chronic active B-cell-receptor signalling in diffuse large B-cell lymphoma. Nature. 2010;463(7277):88-92.

6. Chen L, Monti S, Juszczynski P, Ouyang J, Chapuy B, Neuberg D, et al. SYK inhibition modulates distinct PI3K/AKT- dependent survival pathways and cholesterol biosynthesis in diffuse large B cell lymphomas. Cancer Cell. 2013;23(6):826-38.

7. Advani RH, Buggy JJ, Sharman JP, Smith SM, Boyd TE, Grant B, et al. Bruton tyrosine kinase inhibitor ibrutinib (PCI-32765) has significant activity in patients with relapsed/refractory B-cell malignancies. J Clin Oncol. 2013;31(1):88-94.

8. Fontan L, Yang C, Kabaleeswaran V, Volpon L, Osborne MJ, Beltran E, et al. MALT1 small molecule inhibitors specifically suppress ABC-DLBCL in vitro and in vivo. Cancer Cell. 2012;22(6):812-24.

9. Naylor TL, Tang H, Ratsch BA, Enns A, Loo A, Chen L, et al. Protein kinase C inhibitor sotrastaurin selectively inhibits the growth of CD79 mutant diffuse large B-cell lymphomas. Cancer Res. 2011;71(7):2643-53.

10. Roschewski M, Staudt LM, Wilson WH. Diffuse large B-cell lymphoma-treatment approaches in the molecular era. Nat Rev Clin Oncol. 2014;11(1):12-23.

11. Barua D, Hlavacek WS, Lipniacki T. A computational model for early events in B cell antigen receptor signaling: analysis of the roles of Lyn and Fyn. J Immunol. 2012;189(2):646-58.

12. Ravichandran S, Rao KV, Jain S. Bistability in a model of early B cell receptor activation and its role in tonic signaling and system tunability. Mol Biosyst. 2013;9(10):2498-511.

13. Martinez MR, Corradin A, Klein U, Alvarez MJ, Toffolo GM, di Camillo B, et al. Quantitative modeling of the terminal differentiation of B cells and mechanisms of lymphomagenesis. Proc Natl Acad Sci U S A. 2012;109(7):2672-7.

14. Niiro H, Clark EA. Regulation of B-cell fate by antigen-receptor signals. Nat Rev Immunol. 2002;2(12):945-56.

15. Gauld SB, Cambier JC. Src-family kinases in B-cell development and signaling. Oncogene. 2004;23(48):8001-6.

16. Rolli V, Gallwitz M, Wossning T, Flemming A, Schamel WW, Zurn C, et al. Amplification of B cell antigen receptor signaling by a Syk/ITAM positive feedback loop. Mol Cell. 2002;10(5):1057-69.

17. Baba Y, Hashimoto S, Matsushita M, Watanabe D, Kishimoto T, Kurosaki T, et al. BLNK mediates Syk-dependent Btk activation. Proc Natl Acad Sci U S A. 2001;98(5):2582-6.

18. Kim YJ, Sekiya F, Poulin B, Bae YS, Rhee SG. Mechanism of B-cell receptor-induced phosphorylation and activation of phospholipase C-gamma2. Mol Cell Biol. 2004;24(22):9986-99.

19. Spitaler M, Cantrell DA. Protein kinase C and beyond. Nat Immunol. 2004;5(8):785-90.

20. Shinohara H, Yasuda T, Aiba Y, Sanjo H, Hamadate M, Watarai H, et al. PKC beta regulates BCR-mediated IKK activation by facilitating the interaction between TAK1 and CARMA1. J Exp Med. 2005;202(10):1423-31.

21. Wegener E, Krappmann D. CARD-Bcl10-Malt1 signalosomes: missing link to NF-kappaB. Sci STKE. 2007;2007(384):pe21.

22. Coornaert B, Baens M, Heyninck K, Bekaert T, Haegman M, Staal J, et al. T cell antigen receptor stimulation induces MALT1 paracaspase-mediated cleavage of the NF-kappaB inhibitor A20. Nat Immunol. 2008;9(3):263-71.

23. Hailfinger S, Nogai H, Pelzer C, Jaworski M, Cabalzar K, Charton JE, et al. Malt1-dependent RelB cleavage promotes canonical NF-kappaB activation in lymphocytes and lymphoma cell lines. Proc Natl Acad Sci U S A. 2011;108(35):14596-601.

24. Coughlin JJ, Stang SL, Dower NA, Stone JC. RasGRP1 and RasGRP3 regulate B cell proliferation by facilitating B cell receptor-Ras signaling. J Immunol. 2005;175(11):7179-84.

25. Okada T, Maeda A, Iwamatsu A, Gotoh K, Kurosaki T. BCAP: the tyrosine kinase substrate that connects B cell receptor to phosphoinositide 3-kinase activation. Immunity. 2000;13(6):817-27.

26. Fujimoto M, Fujimoto Y, Poe JC, Jansen PJ, Lowell CA, DeFranco AL, et al. CD19 regulates Src family protein tyrosine kinase activation in B lymphocytes through processive amplification. Immunity. 2000;13(1):47-57.

27. Ding Z, Liang J, Li J, Lu Y, Ariyaratna V, Lu Z, et al. Physical association of PDK1 with AKT1 is sufficient for pathway activation independent of membrane localization and phosphatidylinositol 3 kinase. PLoS One. 2010;5(3):e9910.

28. O'Neill SK, Getahun A, Gauld SB, Merrell KT, Tamir I, Smith MJ, et al. Monophosphorylation of CD79a and CD79b ITAM motifs initiates a SHIP-1 phosphatase-mediated inhibitory signaling cascade required for B cell anergy. Immunity. 2011;35(5):746-56.

29. Zimmermann S, Moelling K. Phosphorylation and regulation of Raf by Akt (protein kinase B). Science. 1999;286(5445):1741-4.

30. Zmajkovicova K, Jesenberger V, Catalanotti F, Baumgartner C, Reyes G, Baccarini M. MEK1 is required for PTEN membrane recruitment, AKT regulation, and the maintenance of peripheral tolerance. Mol Cell. 2013;50(1):43-55.

31. Saito K, Tolias KF, Saci A, Koon HB, Humphries LA, Scharenberg A, et al. BTK regulates PtdIns-4,5-P2 synthesis: importance for calcium signaling and PI3K activity. Immunity. 2003;19(5):669-78.

32. Kang SW, Wahl MI, Chu J, Kitaura J, Kawakami Y, Kato RM, et al. PKCbeta modulates antigen receptor signaling via regulation of Btk membrane localization. Embo J. 2001;20(20):5692-702.

33. Limnander A, Zikherman J, Lau T, Leitges M, Weiss A, Roose JP. Protein kinase Cdelta promotes transitional B cell-negative selection and limits proximal B cell receptor signaling to enforce tolerance. Mol Cell Biol. 2014;34(8):1474-85.

34. Reth M, Brummer T. Feedback regulation of lymphocyte signalling. Nat Rev Immunol. 2004;4(4):269-77.

35. Kumar D, Srikanth R, Ahlfors H, Lahesmaa R, Rao KV. Capturing cell-fate decisions from the molecular signatures of a receptor-dependent signaling response. Mol Syst Biol. 2007;3:150.

36. Kolker E, Higdon R, Haynes W, Welch D, Broomall W, Lancet D, et al. MOPED: Model Organism Protein Expression Database. Nucleic Acids Res. 2012;40(Database issue):D1093-9.

37. McLaughlin S, Wang J, Gambhir A, Murray D. PIP(2) and proteins: interactions, organization, and information flow. Annu Rev Biophys Biomol Struct. 2002;31:151-75.

38. Rameh LE, Cantley LC. The role of phosphoinositide 3-kinase lipid products in cell function. J Biol Chem. 1999;274(13):8347-50.

39. Chen WW, Niepel M, Sorger PK. Classic and contemporary approaches to modeling biochemical reactions. Genes Dev. 2010;24(17):1861-75.

40. Stroppolo ME, Falconi M, Caccuri AM, Desideri A. Superefficient enzymes. Cell Mol Life Sci. 2001;58(10):1451-60.

41. Peters GH, Branner S, Moller KB, Andersen JN, Moller NP. Enzyme kinetic characterization of protein tyrosine phosphatases. Biochimie. 2003;85(5):527-34.

42. Du W, Goldstein R, Jiang Y, Aly O, Cerchietti L, Melnick A, et al. Effective Combination Therapies for B-cell Lymphoma Predicted by a Virtual Disease Model. Cancer Res. 2017;77(8):1818-30.

43. Mathews Griner LA, Guha R, Shinn P, Young RM, Keller JM, Liu D, et al. High-throughput combinatorial screening identifies drugs that cooperate with ibrutinib to kill activated B-cell-like diffuse large B-cell lymphoma cells. Proc Natl Acad Sci U S A. 2014;111(6):2349-54.

44. Bogusz AM, Baxter RH, Currie T, Sinha P, Sohani AR, Kutok JL, et al. Quantitative immunofluorescence reveals the signature of active B-cell receptor signaling in diffuse large B-cell lymphoma. Clin Cancer Res. 2012;18(22):6122-35.

45. Kirouac DC, Du JY, Lahdenranta J, Overland R, Yarar D, Paragas V, et al. Computational modeling of ERBB2-amplified breast cancer identifies combined ErbB2/3 blockade as superior to the combination of MEK and AKT inhibitors. Sci Signal. 2013;6(288):ra68.

46. Assanga I, Lujan L. Cell growth curves for different cell lines and their relationship with biological activities. International Journal of Biotechnology and Molecular Biology Research. 2013;4(4):60-70.

47. Rodriguez-Brenes IA, Komarova NL, Wodarz D. Tumor growth dynamics: insights into evolutionary processes. Trends Ecol Evol. 2013;28(10):597-604.

48. Green TP, Fennell M, Whittaker R, Curwen J, Jacobs V, Allen J, et al. Preclinical anticancer activity of the potent, oral Src inhibitor AZD0530. Mol Oncol. 2009;3(3):248-61.

49. Reilly MP, Sinha U, Andre P, Taylor SM, Pak Y, Deguzman FR, et al. PRT-060318, a novel Syk inhibitor, prevents heparin-induced thrombocytopenia and thrombosis in a transgenic mouse model. Blood. 2011;117(7):2241-6.

50. Honigberg LA, Smith AM, Sirisawad M, Verner E, Loury D, Chang B, et al. The Bruton tyrosine kinase inhibitor PCI-32765 blocks B-cell activation and is efficacious in models of autoimmune disease and B-cell malignancy. Proc Natl Acad Sci U S A. 2010;107(29):13075-80.

51. Wagner J, von Matt P, Sedrani R, Albert R, Cooke N, Ehrhardt C, et al. Discovery of 3-(1H-indol-3-yl)-4-[2-(4-methylpiperazin-1-yl)quinazolin-4-yl]pyrrole-2,5-dione (AEB071), a potent and selective inhibitor of protein kinase C isotypes. J Med Chem. 2009;52(20):6193-6.

52. Bhattarai BR, Ko JH, Shrestha S, Kafle B, Cho H, Kang JH, et al. Inhibition of IKK-beta: a new development in the mechanism of the anti-obesity effects of PTP1B inhibitors SA18 and SA32. Bioorg Med Chem Lett. 2010;20(3):1075-7.

53. Lannutti BJ, Meadows SA, Herman SE, Kashishian A, Steiner B, Johnson AJ, et al. CAL-101, a p110delta selective phosphatidylinositol-3-kinase inhibitor for the treatment of B-cell malignancies, inhibits PI3K signaling and cellular viability. Blood. 2011;117(2):591-4.

54. Burger MT, Pecchi S, Wagman A, Ni ZJ, Knapp M, Hendrickson T, et al. Identification of NVP-BKM120 as a Potent, Selective, Orally Bioavailable Class I PI3 Kinase Inhibitor for Treating Cancer. ACS Med Chem Lett. 2011;2(10):774-9.

55. Feldman RI, Wu JM, Polokoff MA, Kochanny MJ, Dinter H, Zhu D, et al. Novel small molecule inhibitors of 3-phosphoinositide-dependent kinase-1. J Biol Chem. 2005;280(20):19867-74.

56. Yan L, editor MK-2206: A potent oral allosteric AKT inhibitor. Cancer Res; 2009: AMER ASSOC CANCER RESEARCH 615 CHESTNUT ST, 17TH FLOOR, PHILADELPHIA, PA 19106-4404 USA.

57. Stuart D, Aardalen K, Venetsanakos E, Nagel T, Wallroth M, Batt D, et al. RAF265 is a potent Raf kinase inhibitor with selective anti-proliferative activity in vitro and in vivo. AACR; 2008.

58. Yamaguchi T, Kakefuda R, Tajima N, Sowa Y, Sakai T. Antitumor activities of JTP-74057 (GSK1120212), a novel MEK1/2 inhibitor, on colorectal cancer cell lines in vitro and in vivo. Int J Oncol. 2011;39(1):23-31.

59. Kloo B, Nagel D, Pfeifer M, Grau M, Duwel M, Vincendeau M, et al. Critical role of PI3K signaling for NF-kappaB-dependent survival in a subset of activated B-cell-like diffuse large B-cell lymphoma cells. Proc Natl Acad Sci U S A. 2011;108(1):272-7.

60. Lenz G, Wright GW, Emre NC, Kohlhammer H, Dave SS, Davis RE, et al. Molecular subtypes of diffuse large B-cell lymphoma arise by distinct genetic pathways. Proc Natl Acad Sci U S A. 2008;105(36):13520-5.

61. Dobin A, Davis CA, Schlesinger F, Drenkow J, Zaleski C, Jha S, et al. STAR: ultrafast universal RNA-seq aligner. Bioinformatics. 2013;29(1):15-21.

62. Trapnell C, Williams BA, Pertea G, Mortazavi A, Kwan G, van Baren MJ, et al. Transcript assembly and quantification by RNA-Seq reveals unannotated transcripts and isoform switching during cell differentiation. Nat Biotechnol. 2010;28(5):511-5.

63. Scott DW, Wright GW, Williams PM, Lih CJ, Walsh W, Jaffe ES, et al. Determining cell-of-origin subtypes of diffuse large B-cell lymphoma using gene expression in formalin-fixed paraffin-embedded tissue. Blood. 2014;123(8):1214-7.

64. Young RM, Staudt LM. Targeting pathological B cell receptor signalling in lymphoid malignancies. Nat Rev Drug Discov. 2013;12(3):229-43.

65. Singh DK, Kumar D, Siddiqui Z, Basu SK, Kumar V, Rao KV. The strength of receptor signaling is centrally controlled through a cooperative loop between Ca2+ and an oxidant signal. Cell. 2005;121(2):281-93.

66. Shaffer AL, Lin KI, Kuo TC, Yu X, Hurt EM, Rosenwald A, et al. Blimp-1 orchestrates plasma cell differentiation by extinguishing the mature B cell gene expression program. Immunity. 2002;17(1):51-62.

67. Sen R. Control of B lymphocyte apoptosis by the transcription factor NF-kappaB. Immunity. 2006;25(6):871-83.

68. Iwanaga R, Ozono E, Fujisawa J, Ikeda MA, Okamura N, Huang Y, et al. Activation of the cyclin D2 and cdk6 genes through NF-kappaB is critical for cell-cycle progression induced by HTLV-I Tax. Oncogene. 2008;27(42):5635-42.

69. Massague J. G1 cell-cycle control and cancer. Nature. 2004;432(7015):298-306.

70. Mendoza MC, Er EE, Blenis J. The Ras-ERK and PI3K-mTOR pathways: cross-talk and compensation. Trends Biochem Sci. 2011;36(6):320-8.

71. Petrich AM, Leshchenko V, Kuo PY, Xia B, Thirukonda VK, Ulahannan N, et al. Akt inhibitors MK-2206 and nelfinavir overcome mTOR inhibitor resistance in diffuse large B-cell lymphoma. Clin Cancer Res. 2012;18(9):2534-44.

72. Bhalla S, Evens AM, Dai B, Prachand S, Gordon LI, Gartenhaus RB. The novel anti-MEK small molecule AZD6244 induces BIM-dependent and AKT-independent apoptosis in diffuse large B-cell lymphoma. Blood. 2011;118(4):1052-61.

73. Burger JA, Chiorazzi N. B cell receptor signaling in chronic lymphocytic leukemia. Trends Immunol. 2013;34(12):592-601.

74. Boukhiar MA, Roger C, Tran J, Gressin R, Martin A, Ajchenbaum-Cymbalista F, et al. Targeting early B-cell receptor signaling induces apoptosis in leukemic mantle cell lymphoma. Exp Hematol Oncol. 2013;2(1):4.